Activity-dependent gating of parvalbumin interneuron function by the perineuronal net protein Brevican

Emilia Favuzzi[1,2,3], André Marques-Smith[1,2,8], Rubén Deogracias[1,2,3,8], Christian M. Winterflood[4], Alberto Sánchez-Aguilera[1,2], Laura Mantoan[5], Patricia Maeso[1,2,3], Cathy Fernandes[2,6], Helge Ewers[5,7] & Beatriz Rico[1,2,3,9*]

[1]Centre for Developmental Neurobiology, Institute of Psychiatry, Psychology and Neuroscience, King's College London, London SE1 1UL, United Kingdom

[2]MRC Centre for Neurodevelopmental Disorders, King's College London, London SE1 1UL, United Kingdom

[3]Instituto de Neurociencias, Consejo Superior de Investigaciones Científicas & Universidad Miguel Hernández, Sant Joan d'Alacant 03550, Spain

[4]Randall Division of Cell and Molecular Biophysics, King's College London, London SE1 1UL, United Kingdom

[5]Clinical Neurosciences Department, King's College, NHS Foundation Trust, Denmark Hill, London SE5 9RS, United Kingdom

[6]MRC Social, Genetic and Developmental Psychiatry Centre, Institute of Psychiatry, Psychology and Neuroscience, King's College London, London SE5 8AF, United Kingdom

[7]Institute for Chemistry and Biochemistry, Free University Berlin, 14195 Berlin, Germany

[8]Equal contribution

[9]Lead Contact

*Correspondence should be addressed to B.R. (beatriz.rico@kcl.ac.uk)

SUMMARY

Activity-dependent neuronal plasticity is a fundamental mechanism through which the nervous system adapts to sensory experience. Several lines of evidence suggest that parvalbumin (PV+) interneurons are essential in this process, but the molecular mechanisms underlying the influence of experience on interneuron plasticity remain poorly understood. Perineuronal nets (PNN) enwrapping PV+ cells are long-standing candidates for playing such a role, yet their precise contribution has remained elusive. We show that the PNN protein Brevican is a critical regulator of interneuron plasticity. We find that Brevican simultaneously controls cellular and synaptic forms of plasticity in PV+ cells by regulating the localization of potassium channels and AMPA receptors, respectively. By modulating Brevican levels, experience introduces precise molecular and cellular modifications in PV+ cells that are required for learning and memory. These findings uncover a molecular program through which a PNN protein facilitates appropriate behavioral responses to experience by dynamically gating PV+ interneuron function.

INTRODUCTION

Experience-dependent plasticity endows neural circuits in the cerebral cortex with the flexibility required for adapting to a continuously changing environment, thereby contributing to sensory perception, cognition and behavior. The maintenance of precise neuronal coding during fluctuations in activity requires the balanced interaction between excitation and inhibition (Froemke, 2015; Hensch et al., 1998), a process that is dynamically sustained by the function of cortical parvalbumin-expressing (PV+) interneurons (Xue et al., 2014). Although several lines of evidence emphasize pivotal roles for PV+ cells in controlling the gain of sensory-related responses and learning (Wilson et al., 2012; Yazaki-Sugiyama et al., 2009), the molecular and cellular mechanisms by which PV+ interneurons influence these processes are poorly understood.

PV+ cells can adapt their intrinsic properties (cellular plasticity) and outputs (synaptic plasticity) in response to sensory experience. These cells display a remarkable dynamism that allows them to exist in different 'cell states' or configurations, depending on the behavioral context (Bloodgood et al., 2013; Dehorter et al., 2015; Donato et al., 2013; Lagler et al., 2016). While the functional relevance of this novel form of experience-dependent plasticity during behavior is clear (Donato et al., 2013), the molecular mechanisms regulating the adaptability of PV+ interneurons to changing levels of neuronal activity are largely unknown. The lack of information about these processes is particularly striking because PV+ cell dysfunction has been linked to impaired cognition in psychiatric disorders (Cardin et al., 2009; Hu et al., 2014; Sohal et al., 2009). Hence, the identification of the relevant molecular mediators of this form of plasticity may offer novel therapeutic strategies to recover from deficits in perception, learning and memory associated with a repertoire of diseases.

The induction and expression of neural plasticity – cellular and synaptic – relies on complex interactions between neurons and their extracellular environment. The extracellular matrix contains potential candidates for modulating neuronal responses to activity changes. For instance, most cortical PV+ interneurons are wrapped by a specialization of the extracellular matrix known as perineuronal nets (PNNs), that includes chondroitin sulfate proteoglycans (CSPGs) (Deepa et al., 2006). The maturation of PNNs around PV+ cells coincides with the closure of the critical period, a window of enhanced plasticity across different brain regions during early postnatal life (Takesian and Hensch, 2013). It has been suggested that PNNs contribute to this process by promoting synapse stabilization and limiting synaptic rearrangements beyond the critical period for plasticity (Pizzorusso et al., 2002). Consistently, pharmacological degradation of CSPGs in the adult reactivates cortical plasticity and enhances learning (Gogolla et al., 2009). However, in spite of the unequivocal role of PNNs in the regulation of cortical plasticity, the precise mechanism through which PNNs mediate this process remains a mystery.

Brevican (BCAN) is one of the most abundant CSPGs in the brain and a fundamental component of the PNNs (Frischknecht et al., 2014). It is expressed in several brain regions from early postnatal development, mostly inside glial cells and around neurons (Seidenbecher et al., 2002). Though its function is currently unclear, three lines of evidence suggest that BCAN may play a key role regulating experience-dependent plasticity in cortical circuits: (i) BCAN is a component of PNNs surrounding PV+ cells

(Valenzuela et al., 2014); (ii) BCAN is present in cell membranes and synaptosomal fractions (Seidenbecher et al., 2002); and (iii) BCAN is required for long-term potentiation (LTP) in the hippocampus (Brakebusch et al., 2002).

Here we identify the molecular mechanism through which the PNN protein BCAN influences cellular and synaptic plasticity in response to changes in the environment. We demonstrate that BCAN shapes the intrinsic properties of PV+ interneurons and sculpts their synaptic inputs by controlling the localization of potassium channels and the levels of synaptic AMPA receptors, respectively. Moreover, in contrast to the long-standing view that PNN proteins are static and function just as a break for synaptic plasticity (Nabel and Morishita, 2013; Takesian and Hensch, 2013), we show that BCAN is dynamically regulated by activity and that its function is fundamentally required for spatial working and short-term memories. These results therefore reveal that BCAN plays a key role in gating the function of PV+ interneurons, thereby enabling coordinated circuit responses to experience. Our findings clarify the molecular and cellular events underlying the function of PNN proteins in neuronal plasticity.

RESULTS

Brevican is expressed in PV+ interneurons and has a synaptic localization

Brevican protein (BCAN) has been found in several brain regions and its expression is described as a diffuse, dense net-like structure around mostly PV+ cells (Valenzuela et al., 2014). However, the precise source of BCAN remains unclear. We found that in the hippocampus, Brevican transcripts (*Bcan*) are restricted to glial and PV+ cells (Figures 1A-1D and S1A-S1D). BCAN has different splicing isoforms encoding secreted (BCAN1) and GPI-anchored (BCAN2) proteins (Seidenbecher et al., 1995). We observed that whereas both isoforms were co-expressed in glia and PV+ interneurons, the latter population of cells showed a bias towards *Bcan2* expression (Figures 1D-1G). The percentage of PV+ cells that expressed BCAN increased substantially in the second postnatal week, when the maximum fraction of BCAN+/PV+ cells was found (Figures 1H, 1I and S1E). BCAN kept accumulating around PV+ cells after the third postnatal week (Figure S1F). Interestingly, we observed that BCAN+/PV+ cells exhibit higher PV levels than BCAN-/PV+ cells (Figures 1J, 1K and S2A). Of note, although Brevican is also expressed throughout the neocortex (Figures S1G, S1H), no trace of BCAN was detected in chandelier cells (0 out of 9 cells, Figure S1B),

It has been shown that PNNs ensheath synaptic contacts, suggesting a possible role during synapse formation (Hockfield and McKay, 1983). We observed that the frequency and intensity of BCAN staining in PV+ cells increased concurrently with the development of synaptic inputs onto these cells (Figures S1E, S1F, S1I). In the hippocampus, the soma of PV+ basket cells receives both excitatory inputs from pyramidal cells and inhibitory inputs from interneurons. Among these synapses, we found that BCAN was particularly enriched in excitatory terminals (VGlut1+) (Figures 1L-1N). In contrast, only a small percentage of inhibitory puncta (Syt2+ PV+ or GAD65+ PV-) contacting PV+ cells were BCAN+ (Figures S1J-S1O). To analyze the subcellular location of BCAN with nanoscale resolution in hippocampal sections, we developed a novel method for multi-color single-molecule localization-based super-resolution microscopy (Betzig et al., 2006), termed SD-dSTORM (spectral-demixing stochastic optical reconstruction microscopy) (Winterflood et al., 2015) (Figures 1O-1R and S1P-S1S). We first identified somatic synapses apposed to PV+ cells by immunolabeling the synaptic proteins Bassoon (pre-synapse) and Homer1 (post-synapse). As described before (Dani et al., 2010), we observed typical focal planes with Bassoon and Homer1 flanking the synaptic cleft (Figure 1P). Using Bassoon as a reference, we focused on the axial distribution of BCAN and found that it was located both pre- and postsynaptically (Figures 1O-1R). Next, we observed that the average radial position of BCAN relative to the center of the synaptic complex is predominantly peripheral (Figures 1P and 1R). Altogether, our findings reveal that BCAN – mostly BCAN*2* – is expressed in a large fraction of PV+ cells and that it flanks the excitatory synapses received by these cells.

Brevican identifies a subpopulation of PV+ basket cells

PV+ basket cells comprise a highly diverse population of interneurons that integrate in multiple microcircuits and exhibit diverse firing patterns and molecular programs (Dehorter et al., 2015). In addition to the different PV levels exhibited by BCAN+ and BCAN- PV+ cells (Figures 1J, 1K and S2A), using pre- (VGlut1) and postsynaptic markers (PSD95) we found that BCAN+/PV+ cells receive a higher number of excitatory inputs than BCAN-/PV+ cells (Figures 2A-2C and S2B, S2C).

We then enquired whether BCAN+ and BCAN- PV cells could be distinguished on the basis of their electrophysiological properties (Figures 2D-M). BCAN+/PV+ cells are less excitable, showing lower input resistance than BCAN-/PV+ cells (Figures 2I and Table S1). However, BCAN+/PV+ cells also seem better tuned to operate at higher spiking frequencies than their counterparts, as they display higher maximum firing frequency, less spike frequency adaptation, narrower action potential half-width, and an earlier fast after-hyperpolarization (fAHP) time than BCAN-/PV+ cells (Figures 2D-M). Our findings reveal that PV+ cells expressing BCAN have a distinct profile: they receive more glutamatergic synapses, are less excitable and have faster responses than PV+ cells lacking BCAN.

Brevican controls synapses and intrinsic properties of PV+ basket cells

BCAN locates at the flanks of excitatory synapses and its peak of expression coincides with the maturation of these inputs to PV+ cells (Figure S1I). To test a potential function of BCAN in the wiring of PV+ cells, we analyzed the impact of BCAN deletion on the synaptic inputs these interneurons receive. Whereas the density of excitatory synapses impinging on the soma of PV+ cells and the levels of PV expression were comparable in control and *Bcan* mutant mice at early stages of synaptic development (P15), PV+ cells received less excitatory inputs in *Bcan* knockout mice at P30 (Figures 3A-3D and S3A, S3B). Consistently, *Bcan* mutants exhibited a lower frequency – but not amplitude – of miniature excitatory postsynaptic currents (mEPSCs), which also had a slower decay (Figures 3E-3I). These findings indicated that, although BCAN is dispensable for the initial contact of excitatory boutons with PV cells, it is critical for their maturation. Of note, we detected a reduction in PV protein levels at P30 but not at P15, whilst the total density of PV+ cells remained unaltered (Figures 3J-3M and S3C). We observed a similar reduction in the density of excitatory puncta in adult mice (P60, Figures S3D-F), that rules out a potential delay in synapse formation.

To test whether BCAN function is also required for the formation of perisomatic inhibitory synapses in PV+ cells, we examined inputs from other PV+ and Cholecystokinin-positive (CCK+) basket cells (Karson et al., 2009). We observed that the density and size of Syt2+ (a presynaptic marker of PV+ cells) terminals contacting the soma of PV+ cells as well as the density of Syt2+/Gephyrin+ synapses were similar between both genotypes (Figures S3G-S3K). To analyze the contribution of CCK+ interneurons, we combined the GAD65 synaptic protein with the presynaptic receptor CB1, highly enriched in CCK+ axon terminals (Katona et al., 1999) (Figures S3G, S3L-S3N). We found no significant differences in the density of GAD65+/CB1+ synapses between control and *Bcan* mutant mice (Figures S3L-S3N). Consistent with these results, we found no differences in miniature inhibitory postsynaptic currents (mIPSCs) (Figures S3O-S). In agreement with its highly specific location at excitatory synapses, these results revealed that BCAN regulates the maturation of excitatory – but not inhibitory – inputs onto PV+ cells.

Since BCAN+/PV+ cells exhibit different electrophysiological properties than BCAN-/PV+ interneurons, we examined whether loss of BCAN would alter the intrinsic properties of BCAN+/PV+ cells. We found that PV+ interneurons in *Bcan* mutant mice exhibited broader action potentials with smaller fAHP phase (Figures 3N-3V and Table S2). Consistently, the input-output curve was below that of *Bcan*$^{+/+}$ cells (Figures 3V). Moreover, we found that deletion of BCAN enhanced the intrinsic excitability of PV+

cells by decreasing the action potential threshold and latency to first action potential (Figures 3O-3Q and Table S2). To examine how the changes in the excitatory drive and excitability of *Bcan* mutant PV+ interneurons ultimately influenced the flow of information from pyramidal to PV+ cells, we recorded spontaneous excitatory postsynaptic currents (sEPSCs) in PV+ cells (Figures S3T-S3X). We observed a decreased frequency of sEPSCs and slower decay kinetics in *Bcan* mutant mice (Figures S3U and S3X). Our findings therefore demonstrate that BCAN is necessary for the maturation of excitatory inputs onto PV+ interneurons, as well as for the expression of their normative intrinsic properties.

A cell-autonomous function for Brevican in Parvalbumin cells

BCAN is found around the soma of PV+ cells, but its source is unclear, as is its precise cellular contribution to the *Bcan* mutant phenotype. To investigate this, we first explored whether cell-type specific knockdown of BCAN in PV+ interneurons was sufficient to mimic the synaptic and cellular phenotype found in *Bcan* mutant mice. We engineered Cre-dependent conditional constructs expressing a short-hairpin RNA (shRNA) targeting a common region for both *Bcan1* and *Bcan2* (*shBcan*, Figure S4A). We packed this construct in adeno-associated viral vectors (AAV) in which recombination was reported by mCherry (Figures 4A-4C), and the functionality of these constructs was assayed *in vitro* (Figures S4A-F). We co-injected low titer Cre-dependent *shBcan* and YFP-expressing viruses into the hippocampal CA1 region of *PV-Cre* mice at P12 and analyzed the density of synapses in sparsely labeled PV+ cells at P30 (Figures 4A-4G). Expression of *shBcan* led to a loss of BCAN in PV+ cells, causing a decrease in the number of excitatory – but not inhibitory – afferents onto knockdown (mCherry+)

compared to control (YFP+) PV+ cells (Figures 4C-G and S4G-H) and a shift towards lower PV levels (Figure 4H).

We next used a similar approach to explore how PV-specific loss of BCAN affects the intrinsic properties of PV+ cells. We found that PV+ cells that expressed *shBcan* mimicked *Bcan* mutants for some variables but with a stronger trend when compared to *Bcan*$^{+/+}$ mice (Figures 4I-U and Table S3). Altogether, these experiments demonstrated that cell-autonomous expression of BCAN in PV+ interneurons controls their excitatory inputs and some of their intrinsic properties.

Isoform-specific roles for Brevican

To explore which BCAN isoform is required for the maturation of excitatory synapses, we attempted to rescue cell-autonomously the synaptic deficit observed in *Bcan* mutant interneurons by overexpressing Cre-dependent HA-tagged *Bcan1* or *Bcan2* in hippocampal PV+ cells (Figures 5A-C and S4B). HA reported BCAN1 and BCAN2 expression accurately (Figure S5A). Remarkably, whereas BCAN1 resembled other classical PNN markers, BCAN2 expression was dotted, similar to that commonly observed for synaptic markers (Figures 5D, 5I and S5A). We observed that while *Bcan1* expression does not rescue the synaptic phenotype found in *Bcan* mutant PV+ cells, *Bcan2* does (Figures 5E-5H, 5J-5M, S5B-S5G). The synaptic function of BCAN2 required the GPI-anchor, since overexpression of a *Bcan2* that lacks the GPI-domain led to an even more pronounced synaptic phenotype compared to *Bcan-/-* mice (Figure S5D-S5F). Interestingly, both *Bcan1* and *Bcan2* were able to rescue PV levels (Figures 5H and 5M), suggesting that it could change both as a result of modifications in the excitatory drive of PV+ cells as well as by independent cellular mechanisms. Altogether, these results reveal an isoform-specific function for *Bcan2* in the maturation of the excitatory synapses on PV+ interneurons.

Interestingly, we observed a milder reduction of excitatory inputs contacting *Bcan* knock-down compared to *Bcan* knockout PV+ cells (Figures S4G and S5H). Consistently, expression of *Bcan2* in PV+ cells only partially rescued the density of VGlut1+ puncta (Figure S5C). As BCAN is also expressed in glial cells (Figure 1) and astrocytes contribute to synapse development (Clarke and Barres, 2013), we attempted to rescue the *Bcan* mutant PV+ cells wiring phenotype by driving *Bcan1* or *Bcan2* expression in astrocytes (Figures 5N-5X). BCAN1 was secreted from astrocytes, and concentrated around both a small number of PV+ cells (Figures 5Q, 5R and S5I) and few pyramidal cells (Figure S5J), as described before (Carstens et al., 2016). BCAN2 was instead cleaved and released from astrocytes in the tissue without displaying any cell-type bias (Figures 5S and 5T). When expressed in astrocytes, *Bcan2* – but not *Bcan1* –rescued the synaptic phenotype found in *Bcan* mutant PV+ cells (Figures 5U-5X and S5M). However, neither *Bcan1* nor *Bcan2* expression in astrocytes led to a rescue of PV levels (Figure S5L). Altogether, our results suggest that *Bcan2* expression in PV+ cells regulates the maturation of their excitatory inputs, along with a potential contribution from astrocytes.

The marked alteration in the intrinsic properties of PV+ cells upon *Bcan* knock-down suggested a cell-autonomous role for BCAN in the regulation of the firing properties of PV+ cells. To determine whether this was due to the lack of a specific *Bcan* isoform, we asked whether expression of either *Bcan1* or *Bcan2* alone was sufficient to rescue the phenotype found in *Bcan* mutant mice (Figures 5A-C). Our results revealed that none of the two isoforms was by itself sufficient to restore normative intrinsic properties in *Bcan* mutant mice (Figures S5M-W and Table S4), suggesting that either both isoforms may cooperatively regulate the firing behavior of PV+ interneurons or a more complex scenario may be taking place.

Brevican controls AMPA receptors and voltage-gated potassium channels in PV+ cells

Our results demonstrate that BCAN – more specifically, BCAN2 – is necessary for the maturation (Figure 3D) but not initial assembly (Figure S3B) of excitatory synapses onto PV+ cells. These findings prompted us to investigate how BCAN may regulate the differentiation of excitatory synapses.

During postnatal development, neurons edit the composition of their glutamate receptors (Hu et al., 2014). This process is particularly important in PV+ interneurons, where transmission is primarily mediated by GluA2-lacking, calcium-permeable AMPA receptors (AMPARs) with GluA1 and GluA4 subunits (Fuchs et al., 2007; Matta et al., 2013). The slower decay of mEPSCs and sEPSCs found in *Bcan* mutant mice suggested an altered subunit composition of AMPARs (Figures 3I and S3X). To investigate whether BCAN may contribute to the regulation of AMPARs in PV+ cells, we performed co-immunoprecipitation (IP) experiments in hippocampal lysates. We found that BCAN protein co-immunoprecipitated with different AMPAR subunits but not with NMDA or metabotropic glutamate receptors (Figure 6A and S6A). We next examined whether BCAN is required for the expression of GluA1 and GluA4-containing AMPARs at synapses. Analysis of hippocampal synaptosome fractions obtained from *Bcan* mutant mice revealed a reduction of synaptic GluA1 compared to controls (Figures 6B, 6C and S6E). This reduction was accompanied by an increase of GluA1 in the non-synaptic plasma membrane fraction, while no differences were observed in total or cytoplasmic GluA1 protein (Figures 6B, 6C, S6D, and S6E). In contrast, levels of GluA4 were unchanged (Figures S6B and S6C). Interestingly, although *Bcan2* – but not *Bcan1* – is responsible for the synaptic phenotype found in *Bcan* mutants (Figures 5G and 5L), both BCAN1 and BCAN2 co-immunoprecipitated with GluA1 *in vitro* (Figure S6I). Altogether, these results suggested that BCAN may be involved in the trafficking of GluA1 AMPAR subunits from extrasynaptic to synaptic sites.

Since GluA1 subunits are expressed in both pyramidal cells and interneurons, we sought to investigate the neuronal population responsible for the changes in GluA1 subcellular location. Using three-color STORM microscopy in brain sections of wild-type mice, we measured the radial position of BCAN and GluA1 in relation to the synaptic marker Bassoon contacting PV+ cells. We observed that BCAN and GluA1 partially overlap in the outer domain of Bassoon (Figures 6D and 6E). We next analyzed the density of GluA1+ synaptic clusters (Figures 6F-6M and Figure S6F) and found a 50% reduction in *Bcan* mutant and *Bcan* knock-down PV+ cells (Figures 6H and 6L). Cell type-specific loss of GluA1 is in itself sufficient to decrease the excitatory afferents onto PV+ cells, as the density of excitatory synapses was reduced in *PV-Cre;GluA1*$^{F/F}$ mice compared to controls (Figures 6N-6P and S6G). This suggests that the PV-specific loss of GluA1 consequent to disruption of BCAN expression would suffice to produce a deficit in excitatory synaptic inputs. Consistent with the synaptic function of *Bcan2,* only this isoform's expression restored the density of synaptic GluA1+ clusters in *Bcan* mutant PV+ cells (Figures 6I, 6J, and 6M). Our results thus demonstrate that BCAN regulates excitatory inputs contacting PV+ interneurons at least in part by controlling the normal localization and levels of GluA1 AMPAR subunits.

BCAN also regulates the electrophysiological properties of PV+ cells. Some such properties are regulated by fast-activating voltage-gated K^+ conductances mediated by K_v1 and K_v3 potassium channels (Hu et al., 2014). We focused our analysis in the $K_v1.1$ and $K_v3.1$ subunits, which are enriched in PV+ cells and are key for the characteristics of their action potential waveform (Du et al., 1996; Goldberg et al., 2008). We found that both BCAN1 and BCAN2 form protein complexes with $K_v1.1$ and $K_v3.1b$ (Figures S6H and S6I). Consistently, we observed a prominent decrease in the density of $K_v3.1b$ membrane clusters – but not in the total $K_v3.1b$ protein – in *Bcan* deficient PV+ cells (Figures 6Q-6U), which may support deficits in spike waveform, duration and frequency found in the mutants (Figures 3N, 3U, and 3V). We also found a decrease in the density of $K_v1.1$ membrane clusters in PV+ cells – as well as in $K_v1.1$ total protein – in *Bcan* mutant mice (Figures 6V-6Y), a finding that is consistent with the reduction in action potential threshold and latency observed in the mutants (Figures 3O-3Q). BCAN knockdown in PV+ interneurons also reduced the density of $K_v3.1b$ but not $K_v1.1$ clusters in these cells (Figures 6S, 6U, 6X, and 6Z). Altogether, these results suggest that cell-autonomous expression of BCAN in PV+ cells controls fundamental properties of the action potential by regulating the composition of specific channels, including $K_v3.1b$-containing potassium channels.

Brevican expression is dynamically regulated by activity

AMPA glutamate receptors, particularly those containing GluA1 subunits, are recruited to the synapse in an activity-dependent manner (Henley and Wilkinson, 2016) but the molecular mechanisms by which they are trafficked to and held there are not fully understood (Turrigiano, 2012). Since BCAN controls the expression of GluA1 at the synapse, we hypothesized that it might coordinate GluA1 subunit clustering by dynamically responding to changes in activity. To test this idea, we analyzed the expression of BCAN in three different experimental paradigms of altered network activity. First, we used pharmacology in hippocampal cultures: increasing activity with the $GABA_A$ receptor antagonist Gabazine led to a 47% decrease in BCAN levels (Figures 7A and 7B). Reducing activity via L-type calcium channel blockade (Nifedipine) resulted in an increase in BCAN (Figures 7A and 7B).

Second, we obtained tissue from surgical resections of patients with temporal lobe seizures, a pathological model of excessive neural activity. We observed that BCAN was decreased in epilepsy patients compared to controls, suggesting that BCAN levels are controlled by activity also in the human cortex (Figures 7C and 7D). This decrease was not due to a reduction in the number of interneurons, as protein levels for the interneuron marker Lhx6 were similar in both conditions (Figures S7A and S7B).

To confirm that BCAN is dynamically regulated by activity under more physiological conditions, we analyzed changes in BCAN levels associated to training (Figures S7C and S7D). Previous studies have shown shifts in hippocampal PV+ cell network configuration after spatial learning (Dehorter et al., 2015; Donato et al., 2013). Consistently, 4 days of Morris Water Maze (MWM) training caused a shift to low PV expression in PV+ cells (Figure S7E). During the learning phase of the task (day 4), BCAN expression also shifted to lower levels, leading to a decrease in the proportion of BCAN+ cells among the PV+ interneuron population (Figures 7E-7H). Interestingly, upon learning accomplishment (day 10), PV expression shifted to a high-PV network configuration and BCAN expression returned to baseline levels (Figures 7H and S7F-S7H). To strengthen these observations, we analyzed BCAN levels in mice exposed to an enriched environment (EE). We observed that 30 days of EE caused a shift to low PV expression compared to mice housed in standard conditions (Figure S7J). Consistent with a remodeling of the PV+ interneuron network, we also found that EE decreases the levels of BCAN compared to controls (Figures 7I-7K). Consequently, the percentage of BCAN+/PV+ cells was also reduced (Figure 7L). Such changes in the BCAN levels led to synaptic modifications onto PV+ cells (Figure 7M), as observed in *Bcan* mutants (Figure 3). We next demonstrated that both BCAN isoforms were regulated by activity. A decrease in both *Bcan2* and *Bcan1* levels was detected since 4 days of EE (Figures 7N and 7O) when no change in the PV and BCAN levels or in the density of excitatory synapses were yet observed (Figures S7K-S7O). Noteworthy, the reduction of *Bcan2* – but not *Bcan1* – was still maintained after 30 days of EE (Figures 7N, 7O and S7N, S7O). Although both *Bcan* isoforms seem to be regulated by activity, the increase in the *Bcan1*/*Bcan2* ratio suggests that *Bcan2* may be the main isoform that responds to changes in activity (Figure S7P). Altogether, these experiments demonstrate that BCAN levels are dynamically regulated by activity under physiological conditions.

Brevican mutants have cognitive deficits

The activity-dependent dynamics of BCAN could be a critical mechanism for regulating plasticity during learning and behavior. GluA1-containing AMPARs are essential for several hippocampal-dependent forms of memory (Fuchs et al., 2007; Reisel et al., 2002; Sanderson et al., 2009). Since BCAN regulates GluA1 at excitatory synapses contacting PV+ cells (Figure 6), we next examined how the loss of BCAN affects learning and memory (Figures 8 and S8). We assessed spatial working memory on the T-maze and found a moderate impairment in *Bcan* mutant mice (Figures 8A and 8B) that resembles the phenotype of mice lacking GluA1 in PV+ cells (Fuchs et al., 2007).

GluA1 mutants also exhibit impaired short-term spatial memory (Sanderson et al., 2007). To assess whether the lack of BCAN leads to a similar phenotype, we used a novelty preference test on the Y-maze (Figures 8C-H and S8E-S8L) (Sanderson et al., 2007). As expected, control mice showed a strong preference for the novel arm (Figures 8E-7H). In contrast, *Bcan* mutant mice were incapable of discriminating between familiar and novel arms (Figures 8E-8H). Interestingly, when tested for novelty preference after incremental training (Figures S8E-S8L), *Bcan* mutant mice preferred the novel to the familiar arm showing higher discrimination indexes than control mice (Figures S8K and S8L).

In contrast to the short-term deficiencies, long-term memories seem to be enhanced in GluA1 mutants (Fuchs et al., 2007; Sanderson et al., 2009). Thus, we reasoned that alterations in GluA1 subunit mobility due to lack of BCAN might also alter memory consolidation. To explore this possibility, we designed a novel object recognition (NOR) protocol to consecutively assess the effect of BCAN deletion on short-term and long-term memories (Figure 8I-8M and S8M-N). After a short retention interval, we observed that while control mice preferred the novel over the familiar object *Bcan* mutant mice devoted similar time to exploring both novel and familiar objects (Figures 8J, 8K). In contrast, *Bcan* mutants were able to remember the familiar object after a longer retention time and spent more time exploring the novel object (Figure 8L). Interestingly, the discrimination index was higher in *Bcan*$^{-/-}$ mice than in controls (Figure 8M), suggesting potentially enhanced long-term memory in absence of BCAN.

Since BCAN expression in astrocytes may contribute to the synaptic phenotype found in *Bcan*$^{-/-}$ mice (Figure 1), we next investigated whether the specific depletion of BCAN in PV+ cells was sufficient to cause short-term memory defects as observed in *Bcan* mutant mice. *PV-Cre* mice were injected at P12 with Cre-dependent *shBcan-* or control YFP-expressing viruses into the dorsal hippocampus and spatial short-term memory was assessed at P60 by the novelty preference test (Figures 8C, 8D, 8N-8Q and S8O-S8S). We found that *Bcan* knock-down mice displayed the same short-term memory deficit exhibited by *Bcan* mutant mice (Figures 8E-8H and 8N-8Q), demonstrating that normal levels of BCAN specifically in PV+ cells are required for short-term memory. Altogether, these results demonstrate that BCAN regulates plasticity-dependent events that are essential for learning and memory.

DISCUSSION

Several of studies have revealed a critical role for PNNs in experience-dependent plasticity, learning and memory (Gogolla et al., 2009; Pizzorusso et al., 2002). However, how PNNs regulate the function of PV+ interneurons has remained enigmatic. Here we demonstrate that the PNN protein BCAN is expressed by a large fraction of PV+ cells. Expression of BCAN confers PV+ interneurons with specific synaptic and firing properties through the direct regulation of AMPARs and voltage-gated potassium channels. The levels of BCAN vary in response to changes in network activity that are required for learning and memory. Consistently, loss of BCAN leads to deficits in spatial working memory and short-term memory. These results demonstrate that the PNN protein BCAN orchestrates a dedicated molecular program that dynamically gates the drive of PV+ cells and underlies learning and memory.

Since the extracellular matrix (ECM) influences cell-cell interactions, it is conceivable that specific components of the ECM may promote cellular and synaptic plasticity in a cell-specific manner. ECM molecules and associated proteins have been shown to regulate receptor clustering and shape synaptic differentiation, function and plasticity (Chang et al., 2010; Frischknecht et al., 2009; de Wit et al., 2013). In this study, we have shown that PV+ interneurons expressing BCAN receive more glutamatergic inputs than similar cells lacking BCAN. Specifically, expression of the GPI-anchored isoform of BCAN by PV+ cells is responsible for regulating the density of their excitatory synapses. In addition, release of BCAN2 from astrocytes may also contribute to synapse maturation onto PV+ cells. While astrocytes are well-known to critically regulate the development of glutamatergic inputs onto pyramidal neurons (Clarke and Barres, 2013), our results hint at a possible role for these cells at the excitatory synapses of the PV+ interneurons. Future studies will need to address their function on interneuron wiring in more detail. Intriguingly, although our findings show a distinct function for BCAN1 and BCAN2 at the synapses, both BCAN isoforms are able to shift PV levels. One conceivable explanation is that the levels of the calcium binding protein PV change in response to different mechanisms: modifications in both the excitatory drive of PV+ cells that may affect intracellular calcium concentration and in the diffusion of local extracellular calcium. Consistently, PNNs are highly negatively charged and have been proposed to function as a buffering system for cations surrounding fast-firing neurons (Brückner et al., 1993).

BCAN affects excitatory synaptic differentiation, at least in part by modulating the levels of GluA1 receptor at the synapse. In absence of BCAN, GluA1 fails to cluster in postsynaptic densities and this seems to cause a loss of excitatory synaptic contacts onto PV+ interneurons. Since the specific depletion of GluA1 from PV+ cells causes a similar phenotype, it is unlikely that the reduction in GluA1 observed in *Bcan* mutants is due to the loss of synapses by a GluA1-independent mechanism. Nevertheless, it is conceivable that other proteins interacting with BCAN also contribute to the synaptic phenotype described in the present study. Further studies will be needed to elucidate the contribution of other BCAN partners to the maturation of these synapses.

BCAN identifies a dynamic population of PV+ interneurons that not only receives more excitatory synapses but also has distinctive intrinsic properties. PV+ cells expressing BCAN are less excitable, but they are more efficient once recruited. Consistently, we observed deficits in the $K_v1.1$ and $K_v3.1b$ channels in absence of BCAN.

Worth mentioning, in *Bcan* mutants, homeostatic adaptations of PV+ interneurons in response to the decreased number of excitatory inputs seem to trigger changes in Kv1.1. Conversely, a cell-autonomous decrease in Kv1.1 has been previously shown to cause homeostatic changes in connectivity (Dehorter et al., 2015). Altogether, these data support a novel interesting notion that connectivity and cell excitability are reciprocally regulated at the circuit level. Nevertheless, ECM molecules have been implicated in synaptic plasticity through the regulation of ion channels (Kochlamazashvili et al., 2010). As such, BCAN may directly regulate ion channel density, position or function. Indeed, the changes in spike shape and Kv3.1b clustering appear more directly related with the absence of BCAN. Specifically, these properties seem to depend on BCAN expression in PV+ interneurons, as the PV+ cell-specific knock-down revealed a particularly strong and broad phenotype when compared to the full *Bcan* knock-out that might be explained by the different timing of the experimental manipulations. The mature fast-spiking (FS) properties of PV+ interneurons emerge gradually over the first postnatal weeks and are ultimately determined by elaborate interactions among the complements of ion channels that they express (Okaty et al., 2009). Likewise, the first PNNs are observed around P7 and their maturation continues until P28 (Schweizer et al., 1993). In *Bcan* mutant cells, the absence of BCAN during this maturational progression may lead to the compensatory activation of parallel gene expression programs, including the previously reported Neurocan up-regulation (Brakebusch et al., 2002). In *Bcan* knock-down cells, however, BCAN downregulation takes place after the emergence of most of their mature FS physiological features, therefore missing the precise time window for a potential compensation. The presence of developmental adaptations in *Bcan* mutant PV+ cells, might also explain why the relatively late expression of *Bcan1* or *Bcan2* is unable to rescue the electrophysiological phenotype. A complementary explanation is that the presence of both BCAN isoforms is required for PV+ cells to have normal intrinsic properties. Future work addressing the consequences of an earlier *Bcan* deletion and rescue, as well as the developmental emergence of FS properties in *Bcan* mutant PV cells, will help to further decompose the complex electrophysiological phenotype displayed by *Bcan* deficient PV cells.

Growing evidence over the last two decades has shown that the synaptic expression of GluA1 is regulated by activity. For instance, activity-dependent AMPAR insertion at the synapse is the substrate for the expression of the synaptic scaling (Turrigiano, 2012). Interestingly, it was reported that the expression of CSPG proteins requires normal patterns of neural activity (Lander et al., 1997). In the present study, we have shown that BCAN expression is up- or downwardly scaled in response to activity changes. Cortical networks are dynamically regulated by activity *in vivo* (Donato et al., 2013), but little is known about how neurons sense and adapt to the dynamics alterations in network activity at the level of synapses and spiking properties. Recent studies have shown that some of these changes might be mediated by transcription factors (Bloodgood et al., 2013; Dehorter et al., 2015), but the mechanisms through which external signals directly control this process have remained elusive. Here we expose a novel molecular mechanism that simultaneously mediates modifications in the intrinsic properties and synaptic inputs of PV+ interneurons and that is regulated by experience.

Our data provide evidence that BCAN, one of the major components of PNNs, allows PV+ cells to adapt their responses to different types of sensory experience. Specifically, BCAN plays a crucial role in spatial working memory and short-term episodic-like memory but is dispensable, if not obstructive, for long-term memory. How do assemblies of neurons encode and represent different types of memory? It is worth mentioning that BCAN is enriched in the soma and proximal dendrites of PV+ cells, suggesting that it might regulate specific inputs arriving to PV+ cells. Indeed, in the hippocampus, different inputs have distinct subcellular specificity (Klausberger and Somogyi, 2008) and are involved in different aspects of memory (Kitamura et al., 2015). Experience could therefore drive context-specific activation of BCAN+/PV+ cells, where BCAN would contribute to strengthen their excitatory inputs and filter weak and asynchronous stimuli. This positive feedback loop might thus promote the synchronization of pyramidal neurons leading to the formation of short-term memories. On the contrary, prolonged sensory experience, such as that linked to an enriched environment, would attenuate the levels of the PNN protein BCAN. As a consequence, the excitatory drive onto PV+ interneurons would be reduced, further releasing pyramidal cells from inhibition and triggering the plastic rearrangements in the principal cell network that underlie memory consolidation.

A growing amount of research is aiming to reveal the relationship between PNNs, memory and cognition (Tsien, 2013). The newly discovered function of BCAN in PV+ cell plasticity may represent a general principle through which activity-regulated PNN proteins orchestrate selective modifications in specific classes of neurons, thereby influencing network plasticity outcomes upon changes in the environment.

SUPPLEMENTAL INFORMATION

Supplemental Information includes eight figures and five tables.

AUTHOR CONTRIBUTIONS

Conceptualization, E.F. and B.R.; Methodology, E.F., R.D., C.W., B.R.; Formal Analysis, E.F., A.M.S., A.S.A., C.W., Investigation, E.F., A.M.S., R.D., A.S.A., P.M., C.W.; Resources, C.W., C.F., L.M.R., H.E., B.R.; Writing, E.F. and B.R.; Visualization, E.F., A.M.S., C.W., B.R.; Funding Acquisition, B.R.

ACKNOWLEDGEMENTS

We are thankful to N. Carvajal and D. Baeza for technical assistance and lab support, Ian Andrew for mouse management, R. Fässler for *Bcan*$^{-/-}$ mice, S. Arber for *PV-Cre* mice, R. Frischknecht for BCAN antibodies, E. Fuchs, A. Herb and H. Monyer for *PV-Cre;GluA1*$^{F/F}$ brains, A. Navarro for electroporated brains, A. Kirby for helping with the Kv experiments and the London Neurodegenerative Diseases Brain Bank and Brains for Dementia Research (C. Troakes, S. Selvackadunco and S. Al-Sarraj) for human tissue. We are grateful to O. Marín, N. Dehorter, C. Bernard and J. Burrone for critical reading of the manuscript and members of Rico and Marín laboratories for stimulating discussions and ideas. Supported by grants from European Research Council (ERC-2012-StG 310021) to B.R. E.F. was supported by JAE-Pre fellowship (CSIC) and King's College London funds. BR is Wellcome Trust investigator.

FIGURE LEGENDS

Figure 1. Characterization of BCAN expression in the hippocampus at P30.

(A-D) Identification of cell types expressing *Bcan* mRNA. (A-C) PV+ cells, astrocytes and oligodendrocytes among *Bcan*+ cells and percentage (D). *Bcan* common probe for both *Bcan* isoforms, *Bcan1* and *Bcan2* for secreted and membrane-bound isoforms, respectively (n = 3 mice).

(E-G) PV+ cells expressing either (*Bcan1*/*Bcan2*) or both *Bcan* isoforms (*Bcan*) (E and F) and its percentage (G). The diagram in (G) is interprets the data in the bar graph (n = 3 mice).

(H and I) PV+ cells wrapped by BCAN protein (H) and percentage (I) (n = 3 mice).

(J) Image of high-PV BCAN+ and low-PV BCAN- cells.

(K) Cumulative probability plots in BCAN+ (n = 42 cells, 4 mice) and BCAN-PV+ cells (n = 29 cells, 4 mice). Kolmogorov-Smirnov test.

(L-N) VGlut1+ somatic inputs on PV+BCAN+ cells (M-N) and percentage (L) (n = 6 mice).

(O) BCAN+ PV+ cell (conventional wide-field) overlaid with three-color STORM image of BCAN, Bassoon and Homer1. (P) High-magnification images and thresholded masks of O showing single synapses.

(Q) Distribution of BCAN along the trans-synaptic axis. Analysis of 37 side-view synapses from 5 experiments.

(R) Radial distribution of BCAN at the synapse. P(r)/r: probability density of localization at the radial position r. Analysis of 52 face-view synapses from 6 experiments.

Full and open arrowheads show colocalization and no colocalization, respectively. Data are presented as mean. In this and all subsequent figures, error bars represent SEM. Scale bars equal 10 μm (A-D), 20 μm (E, F, H), 5 μm (J and M), 1 μm (N), 2 μm (O), 250 nm (P).

See also Figure S1.

Figure 2. BCAN expression segregates subpopulations of PV+ cells.

(A and B) High magnifications and thresholded masks (A’, B’) showing VGlut1+PSD95+ somatic synapses on the soma of BCAN+ (A) and BCAN- (B) PV+ cells (arrowheads). In A’ and B’ and all subsequent similar images, the opacity of the soma (dotted line) has been reduced to better visualize the synapses.

(C) Density of VGlut1+PSD95+ somatic synapses on BCAN+ and BCAN- PV cells (n = 7 mice).

(D-G) Images and firing traces for BCAN+ (D and E) and BCAN- (F and G) PV+ cells. (H) inset from (E) and (G). NB, Neurobiotin.

(I-M) Intrinsic properties of BCAN+ (n = 22 cells, 9 mice) and BCAN- (n = 13 cells, 9 mice) PV+ cells. AP: Action potential; fAHP: fast after hyperpolarization; Max FF: Maximum firing frequency. Student t-test except for (I) and (K) where Mann-Whitney test was used. In this and subsequent figures $*p < 0.05$, $**p < 0.01$, $***p < 0.001$, n.s., $p > 0.05$. Scale bars equal 1 μm (A, B), 5 μm (D, F).

See also Figure S2 and Table S1.

Figure 3. Deletion of BCAN changes inputs and properties of PV+ cells.

(A-D) Schematic, images, thresholded mask and density of somatic VGlut1+PSD95+ synapses (arrowheads) on PV+ cells (n = 6 WT, 5 *Bcan*$^{-/-}$).

(E-I) Traces, frequency, amplitude, rise and decay time of mEPSCs in WT (n = 12 cells, 4 mice) and *Bcan*$^{-/-}$ PV+ cells (n = 16 cells, 3 mice).

(J-L) Images (J and K) and cumulative probability plots (L) of PV fluorescence intensity in WT (n = 147 cells, 4 mice) and *Bcan*$^{-/-}$ (n = 164 cells, 4 mice).

(M) Density of PV+ cells in the CA1 region of the hippocampus in WT (n = 6) and *Bcan*$^{-/-}$ (n = 4) mice.

(N-U) Intrinsic properties (N-P, R), cumulative probability plot for the spike latency (Q) comparing WT (n = 63 cells, 10 mice) and *Bcan*$^{-/-}$ (n = 41 cells, 6 mice) PV+ cells, firing traces for WT (S) and *Bcan*$^{-/-}$ (T) PV+ cells. (U) inset from S and T.

(V) I/O curves showing the spike frequency of WT (n = 63 cells, 10 mice) and *Bcan*$^{-/-}$ (n = 41 cells, 6 mice) PV+ cells in response to current injections.

Student t-test (D, F, G, I, O and R), Mann-Whitney test (H, M, N and P), Kolmogorov-Smirnov test (L and Q), and two-way ANOVA (V). Scale bars equal 1 μm (B, C), 20 μm (J, K).

See also Figure S3 and Table S1.

Figure 4. Cell-autonomous role of BCAN in PV+ cells.

(A) Schematic of AAVs injections in the hippocampus of P12 *PV-Cre* mice.

(B and C) mCherry and YFP from sparse infection and reduction of endogenous BCAN in *shBcan*-expressing PV+ mCherry+ (full arrowheads) but not mCherry- cells (open arrowheads).

(D) Schematic of BCAN knock-down (KD) PV+ cells in a WT background.

(E-G) Density, images and thresholded masks of VGlut1+PSD95+ somatic synapses on WT (n = 22 cells, 3 mice) and *shBcan* (n = 23 cells, 3 mice) PV+ cells.

(H) Cumulative probability plots (WT, n = 87 cells, 3 mice and *shBcan* PV+ cells, n = 35 cells, 3 mice).

(I-L) Images and firing traces for WT (J, same as in Figure 3S) and BCAN KD (I and K) PV+ cells. (L) inset from (J) and (K). NB, Neurobiotin.

(M-U) Intrinsic properties and cumulative probability plot for spike latency comparing WT (n = 63 cells, 11 mice) and *shBcan* KD (n = 22 cells, 4 mice) PV+ cells.

Student t-test (E, N, Q, S and U), Mann-Whitney test (M, O, R and T), Kolmogorov-Smirnov test (H and P). Scale bars equal 100 μm (B), 20 μm (C), 1 μm (F, G), 10 μm (I). See also Figure S4.

Figure 5. Specific roles for *Bcan* isoforms in PV+ cells and astrocytes.

(A-C) Schematic of AAVs injections (A) and images showing YFP and BCAN1-HA (B) or BCAN2-HA (C).

(D) BCAN1-HA overexpressing cell.

(E-G) Images (E and F) and density (G) of VGlut1+PSD95+ somatic synapses onto *Bcan*$^{-/-}$ (n = 40 cells, 5 mice) and BCAN1 rescued (n = 40 cells, 5 mice) PV+ cells.

(H) Cumulative probability plots (*Bcan*$^{-/-}$, n = 155 cells, 4 mice and BCAN1 rescued, n = 127 cells, 4 mice).

(I) BCAN2-HA overexpressing cell.

(J-L) Images (J and K) and density (L) of VGlut1+PSD95+ somatic synapses on *Bcan*$^{-/-}$ (n = 50 cells, 4 mice) and BCAN2 rescued (n = 34 cells, 4 mice) PV+ cells.

(M) Cumulative probability plots (*Bcan*$^{-/-}$, n = 98 cells, 3 mice and BCAN2 rescued, n = 41 cells, 3 mice).

(N-T) Schematic of AAVs injections (N) and images (O-T) showing CreGFP expression in astrocytes and BCAN1-HA (Q) or BCAN2-HA (S) in the surrounding tissue. P, R and T: high magnification images showing only CreGFP or BCAN1 or BCAN2 accumulation around PV+ cells.

(U-X) Images (U, V and W) and density of VGlut1+PSD95+ somatic synapses on PV+ cells in *Bcan*$^{-/-}$ mice infected with the control virus only (GFAP-CreGFP, n = 6 mice) or together with BCAN1 (n = 4 mice) or BCAN2 (n = 6 mice) virus.

Mann-Whitney test (G, L), Kolmogorov-Smirnov test (H, M), One-Way ANOVA (X). Scale bars equal 100 μm (B, C, O, Q, S), 5 μm (D, I, P, R, T), 1 μm (E, F, J, K, U, V, W). See also Figure S5.

Figure 6. BCAN controls AMPARs and Kv channels.

(A) Co-IP blots from WT hippocampal lysates illustrating pull-down of AMPARs and BCAN (n = 3 mice).

(B and C) Blots and quantification of GluA1 in synaptosomes (S), non-synaptic membranes (M), cytoplasm (C) and total homogenate (H) from *Bcan*$^{-/-}$ and WT mice (n = 6-13 mice per genotype).

(D) Three-color STORM images of BCAN, Bassoon and GluA1 at single synapses onto PV+ cells.

(E) Radial distribution of BCAN and GluA1 relative to Bassoon. Analysis of 117 face-view synapses from 11 experiments.

(F-J) Images and thresholded masks illustrating GluA1+ (full arrowheads) and GluA1- (open arrowheads) excitatory somatic synapses on WT, *Bcan*$^{-/-}$, *Bcan* KD, BCAN1 and BCAN2 rescued PV+ cells.

(K-M) Density of GluA1+ clusters at VGlut1+PSD95+ synapses onto PV+ cells in (K) *Bcan* mutants (n = 5 mice) compared to WT mice (n = 6 mice) and in the cell-autonomous experiments: (L) *Bcan* KD (n = 23 cells, 3 mice) compared to WT cells (n = 22 cells, 3 mice) and (M) BCAN1 (n = 42 cells, 5 mice) and BCAN2 rescued (n = 22 cells, 5 mice) compared to *Bcan*$^{-/-}$ cells (n = 29 cells, 5 mice).

(N-P) Density, images and thresholded masks of VGlut1+PSD95+ synapses (arrowheads) contacting PV+ cells in *PV-Cre; GluA1* conditional mutants (n = 10 mice) compared to controls (n = 6 mice).

(Q and R) Blots and quantification of K_v3.1b in WT (n = 5 mice) and *Bcan*$^{-/-}$ (n = 4 mice) hippocampal lysates.

(S-U) Images and density of K_v3.1b clusters in (T) WT (n = 5 mice) compared to *Bcan*$^{-/-}$ (n = 6 mice) mice and in (U) *Bcan* KD (n = 13 cells, 3 mice) compared to WT cells (n = 23 cells, 3 mice).

(V and W) Blots and quantification of K_v1.1 in WT (n = 9 mice) and *Bcan*$^{-/-}$ (n = 5 mice) hippocampal lysates.

(X-Z) Images and density of K_v1.1 clusters in (Y) WT (n = 5 mice) compared to *Bcan*$^{-/-}$ (n = 5 mice) mice and in (Z) *Bcan* KD (n = 11 cells, 3 mice) compared to WT cells (n = 25 cells, 3 mice).

Student t-test (C, K, L), one-way ANOVA (M), Mann-Whitney test (N, R, T, U, W, Y, Z). Scale bars equal 500 nm (D), 1 μm (F-J, O, P, S, X).

See also Figure S6.

Figure 7. BCAN expression is dynamically regulated by activity.

(A and B) Blots and quantification of BCAN levels in hippocampal cultures treated for 48 hours with vehicle, Gabazine or Nifedipine ($n \geq 7$ wells from 6 independent cultures).

(C and D) Blots and analysis of BCAN protein in the hippocampus of epilepsy patients (n = 4) compared to controls (n = 4).

(E) Cumulative probability plots (control, n = 44 cells, 3 mice; and trained mice, n = 79 cells, 4 mice).

(F and G) Images of BCAN levels in the hippocampus of mice trained for 4 days in the MWM and swimming controls.

(H) Percentage of PV+ cells wrapped by BCAN after 4 days (n = 3 controls and 4 trained mice) and 10 days (n = 4 controls and 4 trained mice) of MWM.

(I) Cumulative probability plots (control, n = 54 cells, 3 mice; and EE mice, n = 71 cells, 3 mice).

(J and K) Images of BCAN level in the hippocampus of mice housed in an EE (K) compared to controls (J).

(L) Percentage of PV+ cells enwrapped by BCAN in control (n = 5 mice) and EE mice (n = 3 mice).

(M) Density of VGlut1+ somatic puncta on PV+ cells in control (n = 5 mice) and EE mice (n = 3 mice).

(N and O) *Bcan1* and *Bcan2* mRNA expression relative to that of GFAP in control (n = 5 mice) and in mice housed in an EE for 4 (n = 5 mice) and 30 (n = 5 mice) days. Scale bars equal 15 μm (F, G, J, K).

Mann-Whitney test (B, D, H, L, M), Kolmogorov-Smirnov test (E and I) and one-way ANOVA (N, O).

See also Figure S7.

Figure 8. BCAN deletion impairs working and short-term memory.

(A) Schematic of the T-maze test.

(B) Percentage of correct responses for wild type (WT, n = 8) and *Bcan*$^{-/-}$ (n = 10).

(C and D) Schematic of the Y-maze test.

(E-H) Number of entries (E), its discrimination index (DI) (F), total time spent (G) and its discrimination index (H) in the "familiar" and "novel" arms for WT (n = 10) and *Bcan*$^{-/-}$ (n = 10) mice.

(I) Schematic of the novel object recognition test.

(J and K) Analysis of short-time recognition memory in WT (n = 19) and *Bcan*$^{-/-}$ (n = 20). Time spent exploring the "familiar" and "novel" object (J). Discrimination index (K).

(L and M) Analysis of long-time recognition memory in WT (n = 18) and *Bcan*$^{-/-}$ (n = 16). Time spent exploring the "familiar" and "novel" object (L). Discrimination index (M).

(N-Q) Number of entries (N), its discrimination index (DI) (O), total time spent (P), and its discrimination index (Q) in the "familiar" and "novel" arms for WT (n = 11) and *Bcan* KD (n = 13) mice in the novelty preference test.

Two-way repeated measures ANOVA (A). One-way ANOVA (E, G, J, L, N, P). Student t-test (F, H, K, M, O, Q). See also Figure S8.

STAR Methods

Contact for Reagent and Resource Sharing

Further information and requests for reagents may be directed to and will be fulfilled by the lead contact, Beatriz Rico (beatriz.rico@kcl.ac.uk).

Experimental Model and Subject Details

Mice

Brevican$^{-/-}$ mice (Brakebusch et al., 2002), *PV-Cre* (Hippenmeyer et al., 2005), *PV-Cre;GluA1*$^{F/F}$ (Fuchs et al. 2007), *VIP-Cre,* and *RCE* (Jackson Laboratories #010908 and #032037), were maintained in a C57B/6 background (Charles River Laboratories); *Nkx2.1CreERT2* mice (Jackson Laboratories #014552) were maintained in a 129S2/SV background and *GIN* mice (Jackson Laboratories #003718) were maintained in a FVB/NJ background. All experimental procedures were performed on male mice, except for the analysis of synapse density in *PV-Cre;GluA1*$^{F/F}$ mice (Figures 6N and S6G) and of the intrinsic properties in *Bcan* knock-down PV+ cells (Figures 4I-4U) where mice of both sexes were used. Animals were maintained under standard, temperature controlled, laboratory conditions, or in an enriched environment with free access to colored tunnels, mazes, climbing materials, and running wheels. Mice were kept on a 12:12 light/dark cycle and received water and food *ad libitum* with the exception of the rewarded alternation test. Animal procedures were approved by ethical committees (IN-CSIC and King's College London) and conducted in accordance with Spanish and European regulations, and Home Office personal and project licenses under the UK Animals (Scientific Procedures) 1986 Act.

Method Details

Perfusions and Immunohistochemistry

Animals were deeply anesthetized with sodium pentobarbital by intraperitoneal injection and then transcardially perfused with PBS followed by 4% paraformaldehyde (PFA) in PBS. Brains were dissected out and postfixed for two hours at 4°C, cryoprotected in a series of sucrose-PBS solutions overnight at 4°C. Then, tissue was sectioned at 40 μm on a sliding microtome (Leica). Free-floating brain sections were permeabilized by incubating with 0.2% Triton X-100 in PBS for 1 hour and then blocked for 3 hours (0.3% Triton X-100, 1% Normal Goat Serum and 5% BSA), followed by incubation with primary antibodies in 0.3% Triton X-100, 1% Normal Goat Serum and 2% BSA overnight at 4°C. The next day, brains were rinsed in PBS and incubated with the appropriated secondary antibodies for 2 hours at room temperature, rinsed in PBS, and then incubated with DAPI. The following primary antibodies were used: mouse anti-parvalbumin (1:1000, Sigma #P-3088), rabbit anti-parvalbumin (1:2000, Swant #PV-25); goat anti-parvalbumin (1:500, Swant #PVG-214); chicken anti-parvalbumin (1:500, SySy #195 006); guinea-pig anti-VGlut1 (1:2000, Millipore #AB5905), mouse anti-PSD95 (1:500, NeuroMab #70-028), guinea-pig and rabbit anti-Brevican (1:1000, a gift from R. Frischknecht), rabbit anti-GluA1 (1:1000, Millipore #04-855), mouse anti-HA (1:500, Covance #MMS-101P), rabbit anti-DsRed (1:500, Clontech #632496), anti-GFP (1:1000, Aves Lab #1020), mouse anti-GAD65 (1:500, Millipore #MAB351R), mouse anti-Synaptotagmin-2 (1:1000, ZFIN #ZDB-ATB-081002-25), goat anti-CB1 (1:400, Frontier Institute # CB1-Go-Af450), mouse anti-gephyrin (1:500, Synaptic Systems #147 011), mouse anti-Kv3.1b (1:1000, NeuroMab #75-041), mouse anti-Kv1.1 (1:500, NeuroMab #75-007).

Fluorescent *In Situ* Hybridization Histochemistry

For dual-color fluorescent in situ hybridization combined with immunohistochemistry, mice were perfused and brains were fixed overnight in 4% PFA in PBS followed by cryoprotection in 30% sucrose-RNase free PBS. 30 μm sliding microtome sections were mounted on RNAse-free SuperFrost Plus slides (Fisher Scientific) with PBST (0.5%Tween20 in PBS), allowed to dry and postfixed in 4% PFA for 5 minutes. After three rinses with PBST, sections were treated with 5 μg/ml proteinase K in PBST (Invitrogen) for 5 minutes, briefly transferred to 4% PFA, and rinsed with PBST. Sections were then incubated for 1 hour at 62°C with hybridization solution (50% formamide, 10% dextran sulfate, 0.2% tRNA, 4% Denhardt's solution, 200 mM NaCl, 10 mM Tris, 5 mM NaH2PO4, 5 mM Na_2HPO_4, 5 mM EDTA, pH 7.5) and hybridized overnight at 62°C with 0.2-0.5 μg of digoxigenin (DIG)-labeled probes diluted in hybridization solution. The next day, sections were rinsed with 50% formamide, 0.5× SSC, and 0.5% Tween 4x30 minutes at 62°C and 1x30 minutes at room temperature. Sections were then blocked for 1 hour in 3% BSA, 20% blocking solution (Roche), 10% sheep serum in MABT (0.1 M maleic acid, 0.2 M NaOH, 0.2 M NaCl, 0.5% Tween) followed by incubation overnight at 4°C with anti-DIG antibody (1:5000; Roche) together with primary antibodies diluted in blocking solution. On the following day, sections were rinsed 12x15 minutes in MABT, incubated with secondary antibodies for 2 hours at room temperature, rinsed 6x5 minutes in PBS, and incubated with DAPI. Sections were then rinsed twice with detection buffer (Tris HCl 100mM, 100 mM NaCl

5M, 10 mM $MgCl_2$ pH 8) and incubated for 3 hours at room temperature in the dark with 2-hydroxy-3-naphthoic acid 2'-phenylanilide phosphate (HNPP)/Fast Red mix (Roche) diluted 1:100 in detection buffer. Sections were rinsed with PBS-EDTA buffer, briefly transferred to 4% PFA, and rinsed twice with PBS. Then, sections were allowed to dry and covered with Mowiol/DABCO. Images were acquired in the following two days on an inverted Leica TCS-SP8 confocal with a 40x objective. The following DIG-labeled probes were used: *Bcan* (IMAGE: 5695027), *Bcan1* (primers: 5'-TGCACCCCTGAGGAGCAAGAC-3' and 3'- CGGGTAAAACCTGAGGCCC TTGTG-5') and *Bcan2* (primers: 5'- GTAATTCTGCTGAAGGCTCAA-3' and 3'-TGGGTACAAAGCAGTTTAATACAG-5'). The probes used to detect the specific *Bcan* isoforms were obtained by RT-PCR amplification of P30 mouse hippocampal cDNA. The purified PCR product was A-tailed and cloned into the pGEMT-easy vector (Promega). The following primary antibodies were used: rabbit anti-parvalbumin (1:500, Swant #PV-25), rabbit anti-Olig2 (1:250, Millipore #AB9610), mouse anti-GFAP (1:500, Sigma #G3893).

Super-Resolution Image Acquisition and Analysis

For super-resolution imaging, mouse brains were fixed overnight in 4% PFA in PBS and cryoprotected in 30% sucrose-PBS. 20 μm sliding microtome sections were stained following immunohistochemistry procedure. The following primary antibodies were used: guinea-pig anti-Brevican (1:1000, a gift from R. Frischknecht), mouse anti-Bassoon (1:500, Abcam #ab82958), rabbit anti-Homer1 (1:400, Synaptic Systems #160 002), rabbit anti-GluA1 (1:1000, Millipore #04-855).

Image Acquisition Single-molecule localization microscopy was performed on a custom-built setup as previously described (Platonova et al., 2015). In brief, a 473 nm laser (100 mW, Laserglow Technologies) was used for activation and a 643 nm laser (150 mW, Toptica Photonics) for imaging. Both lasers were focused onto the back-focal plane of an Olympus NA 1.49, 60x, TIRF-objective. A quad-edge dichroic beamsplitter (405/488/532/635 nm, Semrock) was used to separate fluorescence emission from excitation light. Emission light was filtered by two bandpass emission filters (700/75 nm, Chroma) and a long pass dichroic beamsplitter (690 nm, AHF Analysetechnik) was used to split the emission light. The emission was dually focused by two separate 500 mm tube lenses and onto a back-illuminated EM-CCD chip (Evolve, Photometrics) which was liquid-cooled to -80°C. Focusing was done by moving the objective with a piezo objective positioner (MIPOS100, Piezo Systems Jena). A focus lock was implemented by an electronic feedback loop (LabView, National Instruments), based on total internal reflection of a red laser at the cover slip and its detection on a quadrant photodiode. The z stability was better than ±10 nm over several hours. For SMLM imaging, the switching buffer consisted of 0.1 M MEA/0.2 M Tris, pH 8.0 with 5 % (*w*/*v*) glucose, 0.25 mg/ml glucose-oxidase and 20 μg/ml catalase. The imaging laser intensity of the 643 nm laser line used was ~2 kW/cm ^{2}. To keep the average number of localizations per frame constant (maximum intensity ~0.5 kW/cm^2), the intensity of the 473 nm activation laser was automatically adjusted. Imaging was performed in objective-type total internal reflection fluorescence (TIRF) mode. We recorded a minimum of 30,000 frames with an exposure time of 20-35 milliseconds. All data analysis was performed in MATLAB (Mathworks). The acquired raw camera frames were filtered using a running median filter, a 50 frame filter radius and a keyframe separation of 20 frames. Single-molecule positions were determined by Gaussian fitting based on a maximum likelihood estimator and only localizations with a maximum localization precision of 15 nm and a maximum PSF of 180 nm (1/*e*-intensity) were considered for further analysis. An image-correlation based drift-correction was employed. The first 25 frames of the dSTORM acquisition were used for a coarse estimate of the translational shift between the left and right side of the EMCCD chip. This was done using the phase difference of the Fast Fourier Transform, which was calculated using a pixel-reconstructed image from the single-molecule localization coordinates using a pixel-size of 100 nm. The localizations from the short-wavelength channel were coarsely mapped onto the localizations of the long-wavelength channel and paired. For pairing the localizations of the two channels in each frame had to be within a maximum search-radius of 8 camera pixels (~800 nm). The paired localizations were used to calculate an affine transformation matrix using the MATLAB built-in routine *cp2tform*. The transformation matrix was used to map the localizations from the short-wavelength onto the localizations of the long-wavelength channel. The overall registration precision was 25-35 nm. The localizations were paired again, but using a more stringent cut-off of 1 pixel for the search-radius. The normalized intensity ratio was calculated for all localization pairs for the color-assignment using $r=(I_l-I_s)/(I_l+I_s)$, where I_l and I_s are the fluorescence intensities determined by maximum-likelihood fitting for the long and short wavelength channels, respectively. The localization pair was assigned to AF647, CF660C or C680 by manually selecting the ranges for the normalized intensity ratio. Examples for the dye separation are provided in Figure S1.

Data analysis. Individual synapses contacting the soma of PV cells were manually selected from three-color dSTORM images. To determine the distribution between pre- and post-synaptic site (Figure 1M), "side" view synapses were chosen such that Bassoon and Homer1 were seen as parallel stripes. A line along the center of the pre-synaptic Bassoon was drawn manually (position = 0 nm). The synapses were overlaid with Bassoon = 0 and Homer1 was used to determine the orientation of the synapse. The longitudinal profile of Bassoon/Brevican/Homer1 across the synapse was then determined straightforwardly. For the radial distribution analysis of Bassoon/Homer1/Brevican (Figure 1N) and Bassoon/GluA1/Brevican (Figure 5H), "face" view synapses were chosen such that Bassoon/Homer1 and Bassoon/GluA1 were seen as overlapping round or elliptical discs. The mean x,y position of the Bassoon localizations of each synapse (simplified and considered to be radially symmetric) was set to x,y = 0,0. The Euclidian distance of the Bassoon/Homer1/Brevican and Bassoon/GluA1/Brevican localizations was used to compute their radial distribution for each synapse. The two-color radial distribution analysis of Brevican with respect to Bassoon (Figure S1R) or Homer1 (Figure S1S) was done correspondingly, except that in the latter case the mean x,y position of Homer1 localizations was used to establish x,y = 0,0.

Cell Culture, Transfection, Pharmacology and Immunocytochemistry

Cell line cultures. HEK293FT cells were cultured in Dulbecco's Modified Eagle's medium supplemented with 10% fetal bovine serum, 2 mM glutamine, penicillin (50 units/ml) and streptomycin (50 g/ml). The cultures were incubated at 37°C in a humidified atmosphere containing 5% CO_2. HEK293FT cells were transfected using polyethylenimine (PEI, Sigma) at a 1:4 DNA:PEI ratio.

Primary hippocampal cultures. Hippocampi from E18 mouse embryos (both sexes) were dissected in ice-cold Hank's Balanced Salt Solution (HBSS), digested with 1 mg/ml trypsin (Worthington) for 15 minutes at 37°C, treated with 0.1 mg/ml DNase I (Roche) and triturated to produce a single cell suspension. Cells were then plated at 100,000 cells/cm^2 on plastic dishes. Cells were cultured in Neurobasal (Invitrogen) supplemented with 2% B27 (Invitrogen), glutamine (2 mM) and 100 μg/ml penicillin-streptomycin (Gibco). For *in vitro* activity manipulations, 26DIV neuronal cultures were treated for 48 hours with 20 μM Gabazine or 20 μM Nifedipine, or their appropriated controls (H_2O, and DMSO, respectively).

Immunocytochemistry. HEK293FT cells were fixed in 4% PFA/1% sucrose in PBS for 10 minutes, briefly washed in PBS and permeabilized with 0.2% Triton X-100 in PBS. Coverslips were blocked with 5% BSA in PBS for 1 hour and incubated with primary antibodies in blocking solution overnight at 4°C. Coverslips were then washed 6x5 minutes in PBS and incubated with secondary antibodies in blocking solution for 1h at room temperature. Coverslips were then washed 6x5 minutes in PBS, incubated with DAPI and mounted in Mowiol/DABCO. Primary antibodies used: chicken anti-GFP (1:3000, Aves Lab #1020), guinea-pig anti-Brevican (1:2000, a gift from R. Frischknecht), rabbit anti-Brevican (1:2000, a gift from R. Frischknecht), rabbit anti-DsRed (1:500, Clontech #632496), mouse anti-HA (1:500, Covance #MMS-101P).

Generation of AAV Expression Vectors

To generate the *pDIO-shBCAN-mCherry*, the sequence containing the distal and proximal elements of the U6 promoter spaced by the CDS for mCherry was amplified by PCR. The resulting PCR product was cloned into the *pAAV-EF1a-DIO-mCherry* vector (a gift from Prof. K. Deisseroth, Addgene plasmid #20299) and a TATA box was introduced in the U6 fragment (primer sequences and cloning details will be provided elsewhere). The ssDNA primers to generate the shBCAN (5’-CTAGGCAAGCAGAACCGCTTCAATGCCTGACCCACATTGAAGCGGTTCTGTTGCTTTTTG-3’ and 3’-AATTCAAAAAGCAAGCAGAACCGCTTCAATGTGGGTCAGGCATTGAAGCGGTTCTGCTTGC-5’) were obtained using the Block-it RNAi web tool (Thermo Scientific). To minimize the putative off-target effects of the shRNA, a miR-133 derived loop sequence was used (Gu et al., 2012). Moreover, the shRNA sequence was blasted and no other mouse mRNA apart from *Bcan* was predicted to be targeted. The coding sequences for *Bcan1* and *Bcan2* full-length used in the rescue experiments were obtained from P30 mouse hippocampal cDNA and cloned into the pGEMT-easy vector (Promega). A canonical HA tag sequence was introduced after the signal peptide (primers: 5’-TCTAGAGCCACCATGATACCACTGCTTCTGTCCCTGCTGGCCGCTCTGGT-3’ and 3’-TTGGGTCAGGACCAGAGCGGCCAGCAGGGACAGAAGCAGTGGTATCATGGTGGCCTAGAA-5’; 5’-CCTGACCCAAGCCCCTGCCGCCCTCGCTGATTACCCATACGATGTTCCAGATTACGCTAGATCTA-3’ and 3’-AGATCTAGCGTAATCTGGAACATCGTATGGGTAATCAGCGAGGGCGGCAGGGGC-5’) and cloned in the *pAAV-EF1a-DIO-mCherry* vector. To generate a *Bcan2* mutant that lacks the GPI anchor (BCAN2-GPI), the DNA sequence coding for the protein region containing the C-terminal GPI-modification sites was removed from

Bcan2 full-length (P**S**SGNSAEGSMPAFLLFLLLQLWAT, best predicted site is shown in bold and is underlined, the alternative site is underlined).

AAV Production and Intracranial Injections

HEKs 293FT cells (ThermoScientific) were seeded on 15-cm plates and co-transfected with packaging plasmids AAV-ITR-2 genomic vectors (7.5μg), AAV-Cap8 vector pDP8 (30μg; PlasmidFactory GmbH, Germany, #pF478) using PEI (Sigma) at a ratio 1:4 (DNA:PEI). 72 hours post transfection, supernatants were incubated with ammonium persulfate (65g/200ml supernatant) for 30 minutes on ice and centrifuged for 45 minutes at 4000 RPM at 4°C. Transfected cells were harvested and lysed (150mM NaCl, 50mM Tris pH8.5), followed by three freeze-thaw cycles and Benzonase treatment (50U/ml; Sigma) for 1 hour at 37°C. Filtered AAVs (0.8 μm, 0.45 μm and 0.2 μm MCE filters) from supernatants and lysates were run on an iodixanol gradient by ultracentrifugation (Vti50 rotor, Beckmann Coultier) at 50,000 RPM for 1 hour at 12°C. The 40% iodixanol fraction containing AAV was collected, concentrated using 100 kDa-MWCO Centricon plus-20 and Centricon plus-2 (Merck-Millipore), aliquoted and stored at -80°C. The infectious titer of virus was measured by quantitative real-time PCR (primers: 5’-GGCACTGACAATTCCGTGGT-3’ and 3’-CGCTGGATTGAGGGCCGAA-5’). AAVs with a titer equal or higher to 10^{11} genome copy/ml were used for in vivo injections. The AAV9-EF1a-DIO-eYFP was generated by and acquired from the Penn Vector Core, with a titer of 3.95 x 10^{13} genome copy/ml. The AAV8-GFAP(0.7)-EGFP-T2A-iCre was generated by and acquired from the Vector Biolabs, with a titer of 5.6 x 10^{13} genome copy/ml.

For intracranial injections, P12 mice were anesthetized with isoflurane and were mounted in a stereotactic frame. For synapse analysis, 250 nl of AAV8-shBcan-mCherry:AAV9-YFP in a 10:1 ratio, AAV8-Bcan1-HA:AAV9-YFP in a 10:1 ratio, AAV8-Bcan2-HA:AAV9-YFP in a 10:1 ratio, AAV8-Bcan2-HA:AAV8-GFAP-iCRE in a 1:1 ratio or AAV8-Bcan2-HA:AAV8-GFAP-iCRE in a 1:1 ratio were unilaterally injected into the dorsal region of the left hippocampus (anteroposterior −2.8 mm; mediolateral +1.2 mm; dorsoventral −1.3 mm relative to Bregma) at an injection rate of 50 nl/minute followed by 2 additional minutes to allow diffusion.

For electrophysiology or behavioral experiments we performed injection of high titer Cre-dependent viruses. Specifically, 400 nl of AAV8-shBcan-mCherry:AAV9-YFP in a 10:1 ratio, 400 nl of AAV8-Bcan1-HA:AAV9-YFP in a 10:1 ratio or 400 nl AAV8-Bcan2-HA:AAV9-YFP in a 10:1 ratio (for electrophysiology experiments) or 500 nl of AAV8-shBcan-mCherry or 500 nl of AAV9-YFP (for behavioral experiments) were bilaterally injected into the dorsal region of the hippocampus (anteroposterior −2.5, −2.8, −3.2 mm; mediolateral +1.2 mm; dorsoventral −1.3 mm relative to Bregma) at an injection rate of 100 nl/minute. Post-recording immunocytochemistry was carried out to evaluate the recorded cell and/or the expansion of the injection. For behavior, the injections massively targeted the majority of the PV cells in the dorsal hippocampus (data not shown).

Western blot and Fractionation

For Western blot analysis on neuronal cultures, DIV28 E17.5 hippocampal cultures or HEK293FT were placed on ice and rinsed 1x in PBS. For Western blot analysis on mouse tissue, P30 hippocampi were rapidly dissected in ice cold PSB. Samples were homogenized in lysis buffer containing 25 mM Tris-HCl pH 8, 50mM NaCl, 1% Triton X-100, 0.5% sodium deoxycholate, 0.001 % SDS and protease inhibitor cocktail. For anti-Brevican Western blot, samples were digested with 1.7U/mg of ChABC (Sigma) for 2 hours at 37°C. For fractionation experiments, Syn-PER™ Synaptic Protein Extraction Reagent (ThermoScientific) or Subcellular Protein Fractionation Kit for Tissues (ThermoScientific) were used according to the manufacturer's instructions. Protein quantity was measured using bicinchoninic acid (BCA) assay (ThermoScientific). All samples were denatured, resolved by SDS-PAGE and transferred onto PVDF membranes. Membranes were blocked with 5% nonfat milk (Biorad) in TBST (20mM Tris-HCl pH7.5, 150mM NaCl and 0.1% Tween20) for 1 hour and probed with the following primary antibodies: mouse anti-PSD95 (1:500, NeuroMab #70-028), guinea-pig and rabbit anti-Brevican (1:1000, a gift from R. Frischknecht), rabbit anti-actin (1:1000, Sigma #A2066), rabbit anti-GluR1 (1:1000, Millipore #04-855), mouse anti-GAPDH (1:1000, Sigma # G8795), rabbit anti-T-cadherin (1:500, Millipore #ABT121), rabbit anti-Na,K-ATPase (1:1000, Abcam, #ab76020), mouse anti-HA (1:500, Covance #MMS-101P), mouse anti-Kv1.1 (1:500, NeuroMab #75-007). After incubation with HRP-conjugated secondary antibodies, protein levels were visualized by chemiluminescence. Blots were scanned using a LI-COR Odyssey® Fc Imaging System and band were quantified with Image Studio Software. For quantification, densitometry of protein bands of interest was normalized to that of actin.

Co-immunoprecipitation Assays

100 μg of hippocampal homogenates from P30 mice or, for Brevican isoform-specific Co-IP, 100 μg of hippocampal homogenates from P30 *Bcan* mutant mice were mixed

with 50 μg of lysate from HEK293FT co-transfected with CreGFP and a Cre-dependent Bcan1-HA or Bcan2-HA expressing plasmid were used. The lysate was then diluted in 1 ml of Co-IP buffer (0.3M sucrose, 10 mM Tris-HCl pH 8, 10 mM NaCl, 3 mM $MgCl_2$, 1% NP-40, 5% glycerol and protease inhibitor cocktail) and subsequently incubated overnight at 4°C with 2 μg of one of the following antibodies: rabbit anti-GluR1 (Millipore #04-855), rabbit anti-GluR2-3 (Millipore #AB1506), rabbit anti-GluR4 (Millipore #AB1508), rabbit anti-NMDAR2B (Millipore #AB1557P), Rabbit IgG-Isotype Control (Abcam #ab27478), rabbit anti-mGluR2-3 (Millipore #AB1553), mouse anti-Kv1.1 (NeuroMab #75-007), mouse anti-Kv3.1b (NeuroMab #73-041), Mouse IgG-Isotype Control (Abcam # ab37355). 50 μl of protein A-Sepharose (Sigma) bead slurry was washed in Co-IP buffer and added to the mixture. After overnight incubation at 4°C with gentle rotation, the beads were pelleted and rinsed three times with Co-IP buffer. Immune complexes were then analyzed by western blot.

In vitro **Patch Clamp Recordings**

Slice preparation. Postnatal day (P) 26-38 mice were deeply anesthetized with sodium pentobarbital and transcardially perfused with ice-cold sucrose-based cutting solution containing (in mM): 70 Sucrose, 86 NaCl, 4 KCl, 1 NaH_2PO_4, 7 $MgCl_2$, 26 $NaHCO_3$, 25 Glucose and 0.5 $CaCl_2$. After brain dissection, 300 μm coronal hippocampal slices were cut using a vibratome (Leica) in the same ice-cold solution. After cutting, slices were transferred to an incubation chamber filled with artificial cerebrospinal fluid (ACSF) heated to 34 ˚C and containing (in mM): 127 NaCl, 2.5 KCl, 0.6 NaH_2PO_4, 26 $NaHCO_3$, 13 Glucose, 1.3 $MgSO_4$, 2 $CaCl_2$. Slices were kept in this heated chamber for 30 minutes and then transferred to a second chamber containing the same solution at room temperature, where they were kept for an additional 30 minutes, and throughout the day, before recordings.

Patch clamp recordings. After recovery, slices were transferred to a recording chamber continuously superfused with ACSF heated to 34 ˚C. PV interneurons were viewed with infrared-differential interference optics (Hamamatsu camera controller) and fluorescence illumination (Cool Led 473nm) through a 40x water-immersion objective (Olympus). Patch microelectrodes (4–8 MΩ) were pulled from borosilicate glass (1.5 mm outer diameter x 0.86 mm inner diameter; Harvard Apparatus) using a vertical P10 puller (Narishige). Current-clamp and voltage-clamp (sEPSC) recordings were performed using an intracellular solution containing, in mM, 130 KGluconate, 5 KCl, 10 HEPES, 2 MgCl2, 10 Sodium Phosphocreatine, 2 Na2-ATP and 0.4 Na-GTP, as well as 1mg/ml neurobiotin. sEPSCs were recorded at a holding potential of -70 mV. During current-clamp recordings, membrane potential was biased towards -65 mV. Cells were kept under current-clamp or voltage-clamp configuration with a Multiclamp 700B amplifier operating in fast mode. For mEPSC and mIPSC recordings, the following intracellular solution was used (in mM): 135 Cesium Methanesulfonate, 8 KCl, 10 HEPES, 0.4 Mg-ATP, 2.0 Na2-ATP, 0.5 EGTA, 0.6 Na-GTP. 1 μM TTX was added to the bath. mEPSCs were recorded at -60 mV and mIPSCs at +10 mV, accounting for an estimated liquid-junction potential of 10.4 mV. No pharmacological blockade of transmission was performed, in order to allow recording mEPSCs and mIPSCs from the same cell. Data were filtered on-line at 2 kHz, and acquired at a 20 kHz sampling rate for current-clamp recordings in Figure 2 and 50kHz for all others using pClamp 10.7.0 software (Molecular Devices). For immunohistochemistry after patch clamp recording, slices were immediately drop-fixed in PFA 4% at room temperature for 30 mins and subsequently transferred into PBS with 0.05% sodium azide. For BCAN+ and BCAN- cells, only one cell was recorded per slice, as to allow for unequivocal identification between immunohistochemical staining and electrophysiological recording.

Data analysis. Intrinsic properties were measured rapidly after obtaining whole-cell configuration, through injection of a series of depolarizing or hyperpolarizing 500 milliseconds current steps were used at 0.5 Hz. Resting membrane potentials were measured just after patched membranes were ruptured by suction. Input resistance and membrane time constants were determined by passing hyperpolarizing current pulses inducing voltage shifts of 5-15 mV negative to resting membrane potential. Time constants were measured by fitting voltage responses with a single exponential function. Action potential (AP) threshold was determined as the voltage at which slope trajectory reached 20 mV/milliseconds. AP widths at half amplitude were measured for spikes elicited by depolarizing current pulses of threshold strength. Rheobase was determined by initially injecting positive current generating near-threshold 15-25 mV depolarizations and subsequently applying 1 pA current steps until APs were elicited. Rheobase was considered to have been reached once three such steps consecutively produced an AP, with the lowest value of the AP-generating injected currents used. Delay to first AP was measured during the same procedure, as the time elapsed between onset of current injection and AP threshold and was calculated from the average of 4 repetitions of this procedure. AP height was calculated as the difference in membrane potential between AP threshold and the peak. Afterhyperpolarisation (AhP) amplitude was defined as the difference between AP threshold and the most negative potential attained within 5 milliseconds of AP threshold. AhP time was defined as the time elapsed between this point and AP threshold. For *Bcan*$^{-/-}$ recordings, since a change in AP threshold occurred, we corrected AhP amplitude accordingly. Saturating firing frequency and input-output curves were obtained by injecting steps of 100 pA current and counting spike number. AP frequency adaptation was calculated as the percent change in spike frequency during the last 100 milliseconds of the spike train compared to the first 100 milliseconds. Synaptic currents were analysed semi-automatically with Mini-Analysis (Synaptosoft), using detection parameters of 7 pA for event threshold, 10 ms for searching for a local maximum, 5 ms to search for baseline before peak, 50 ms to search for decay time and 0.37 as the fraction of peak amplitude to find a decay time. Rise-time was calculated as time elapsed between 10 and 90% of peak amplitude.

Image Acquisition and Analysis

Samples belonging to the same experiment were imaged during the same imaging session on an inverted Leica TCS-SP8 confocal. Imaging was performed with the same laser power, photomultiplier gain, pinhole and detection filter settings (1024x1024 resolution, 12 bits or 16 bits). For cell co-localization analyses, confocal image stacks (40X oil immersion objective, 1.4 NA, 0.2 μm step size) were used to create maximum intensity projections and analyzed using a custom macro in Fiji (ImageJ) software. For Brevican and PV level analyses, Cy3 and AF647 fluorophores were used, respectively, and confocal image stacks (40X oil immersion objective, 1.4 NA, 0.2 μm step size) were reconstructed and analyzed with IMARIS 7.5.2 software. PV neurons whose soma was included within the tissue sections with optimal staining were isolated in three dimensions. Three-dimensional isosurfaces were created around each PV-neuron soma using the “create surface” tool and volume and labeling intensities were quantified automatically. A threshold was selected to include as much of the neuron as possible while excluding any background. A size filter was applied with the minimum size being related to the volume of the PV cell. The PV surface was then used to define the cellular domain and create three-dimensional isosurfaces around the PV neuron in the Brevican channel. The threshold was selected so as to have no surface reconstruction outside the cellular domain of PV cells. Brevican volume and intensity were quantified automatically. For synaptic puncta/cluster analysis, images of z-planes with optimal staining of synaptic markers were acquired (100X oil immersion objective, 1.44 NA, 2.2 digital zoom). Analysis of excitatory and inhibitory synapses contacting PV cells was carried out in the stratum oriens of the CA1 region of the hippocampus. Analysis of synaptic puncta/cluster densities was performed using a custom macro in Fiji (ImageJ) software. Processing of all channels included background subtraction, Gaussian blurring, smoothing and contrast enhancement. All single channel images were converted to RGB. For the PV soma, a color threshold was selected to identify the cell soma. The border of the soma was automatically or manually drawn to automatically calculate its perimeter and create a mask with the cell body only. For the presynaptic boutons or postsynaptic clusters, a color threshold was selected to include as many putative synapses as possible while excluding any background. The same threshold in each channel was applied to all images from the same experiment. The “Analyze Particles” (size 0.10-infinity, circularity 0.00-1.00) and “Watershed” tools were applied and a mask was generated. A merged image from all masks was created. Presynaptic boutons were defined as such when they were located outside the perimeter border but had ≥ 0.1 μm^2 colocalizing with the mask of the soma. The criterion to define postsynaptic clusters was that ≥ 0.2 μm^2 of the cluster area in the mask was located inside the perimeter border of the soma. Synapses were counted when an identified postsynaptic cluster was contacted by a presynaptic terminal (i.e. they had ≥ 1 pixel colocalizing) or when an identified presynaptic bouton was contacting (i.e. they had ≥ 1 pixel colocalizing) a postsynaptic cluster with ≥ 1/4 of its area located inside the perimeter border of the soma. For the four-color analysis of GluA1-containing synapses, GluA1 clusters in PV cells were considered located at the synapse when colocalising with a PSD-95 postsynaptic cluster that was contacted by a VGlut1 presynaptic terminal. For the correlation analysis shown in Figure S2B, confocal image stacks (100X oil immersion objective, 1.4 NA, 2.2 digital zoom, 0.2 µm step size) were reconstructed and analyzed with IMARIS 7.5.2 software. The PV cell soma was reconstructed with the "create surface" tool as described above. The VGlut1 presynaptic boutons and the Brevican coats were detected with the "spot" tool using a spot diameter of 0.68 µm for the VGlut1 boutons and of 0.5 µm for the Brevican coats. A threshold was selected to accurately detect as many spots as possible without creating artifacts. The radius of the spot was used as a threshold distance to define the contact and the "Find spots close to surface" tool (ImarisXT extension) was then used to count the number of presynaptic VGlut1 and Brevican spots that were contacting the surface of the soma.

In utero electroporation and Tamoxifen Induction

CA1 pyramidal cells were labeled by in utero electroporation of a GFP plasmid in *NEX-Cre* mice. Pregnant females were anesthetized with isofluorane. The uterine horns were exposed and embryos were injected through the uterus wall using pulled capillaries filled with DNA (1.5 µg µl-1) diluted in PBS and colored with Fast Green (0.5%) (Sigma).

Brain ventricles were filled with DNA solution (pCAGGS-IRES-GFP or pCAGGS-CRD-Nrg1-IRES-GFP) and electroporated (CUY21/CUY650P3/ CUY650P5, Nepa Gene Co.) using a program of 45 V, 50 ms, 950 ms, and five pulses.

Tamoxifen was dissolved in corn oil (10 mg/ml) at 37°C with constant agitation. Chandelier cells (ChCs) were labeled by intra-gastric tamoxifen injections of P2 post-natal *Nkx2.1CreERT2;RCE* mouse pups at a dose of 1mg/10g of body weight.

Quantitative real-time PCR

Total RNA was extracted from mouse hippocampi using TRIzol reagent (Invitrogen) followed by DNAse I treatment (Promega). cDNA synthesis was performed using the SuperScript IV First-Strand Synthesis System (Invitrogen) according to the manufacturer's protocol. qPCR was carried out in triplicates on a LightCycler 480 Instrument (Roche) using SYBR Green PCR Master Mix (Roche). Normalized mRNA levels for *Bcan1* and *Bcan2* relatively to those of *Syt2* or *Gfap* were calculated using the comparative C_T method. The sequences of qPCR primers were as follows: *Bcan1* (Fw: CTATGTTTGCCAGGCTATGGGGG, Rv: TGCCTCCTCCCAACTCCTTCGTG), *Bcan2* (Fw: GTCCTGGCAGGCACCTCAGTG, Rv: GCATTGAGCCTTCAGCAGAA TTAC), *Syt2* (Fw: ACGTGCCCACAGCTGGGAAGCTC, Rv: GTCTCTTACCGTTCT GCATCAGG), *Gfap* (Fw: GGGACAACTTTGCACAGGACCTC, Rv: GGTGGCTTC ATCTGCCTCCTGTC). The activity-dependent gene *Npas4* (Fw: TTCAAGCCAAG CATGGAGGCTGG, Rv: TAGCTGCTGGCGGAGGCTCC AGG) (Bloodgood et al., 2013), was used to confirm the increase in activity in the enriched environment experiment.

Epilepsy human samples

Frozen postmortem brain tissue from individuals with epilepsy and controls was kindly supplied by the MRC London Neurodegenerative Diseases Brain Bank. Brain tissue of both sexes and age between 54 and 80 years old was used in the study. Control brains were from individuals with no history of epilepsy or psychiatric disease. The use of human sections was covered by ethics approval granted to the London Neurodegenerative Diseases Brain Bank. For biochemical analysis, 50 μg of tissue from the CA1 region of the hippocampus were homogenized in lysis buffer and processed following Western blot procedures as described above.

Behavioural procedures

Animals were maintained under standard, temperature controlled, laboratory conditions and kept in 12 hours light-dark cycles with *ad libitum* access to food and water with the exception of the rewarded alternation test. For all behavioral tests, mice were housed singly and assessed during the light phase of the day.

Enriched environment. C57BL/6J male mice were housed together for 4 days (8-week old mice) or 1 month (4-week old mice) in an enrichment cage composed of colored tunnels, mazes, climbing materials, and tilted running wheels (Marlau Cage, ViewPoint Behavior Technology). Controls were age-matched littermates housed in standard conditions.

Morris Water Maze. Testing of 8-12 weeks old C57BL/6J (n = 10) was performed in a 130-cm pool filled with milky water, surrounded by four different objects placed as reference cues onto white curtains. A circular escape platform (10 cm diameter) was submerged 0.5 cm below the water surface. Mice were trained to find the platform during four trials a day, with inter-trial intervals of 5 minutes spent in their home cage. During training, mice were released from pseudo-randomly assigned start locations; they were allowed to swim for up to 60 seconds and they were manually guided to the platform in the case of failures. Performance was scored as the average latency to find the platform in the four consecutive trials each day. On the last day, the reference memory was assessed as fraction of time spent in the target quadrant during one full trial (60 seconds) upon removal of the escape platform. Swim controls (n = 8) were age-matched mice that were allowed to swim in the pool without escape platform, in a comparable training regime (four trials per day; inter-trial intervals of 5 minutes). For swim controls, trial durations for each day were adjusted to average values of training animals. Trials were tracked using EthoVision software (Noldus Information Technology).

Rewarded alternation task in T-maze. Mice were maintained on a restricted feeding schedule at 85% of their free-feeding weight. Spatial working memory was assessed on a continuous black T-maze consisting of a start arm (60 x 10 cm), two identical goal arms (35 x 10 cm) and two return arms (90 x 10 cm), surrounded by a 14 cm high wall. Light sources in the room were adjusted in order to have the same light intensity in every arm of the maze (20 LUX) and the maze was surrounded by various prominent distal extra-maze cues. The mice were habituated to the maze and to drinking condensed milk pellets over two days for 8 minutes every day. After habituation, animals were pre-trained daily over several days until the consumption of the reward reached minimum 80%. Each pre-training daily session consisted of 4 trials and mice were run one trial at a time with an inter-trial interval (ITI) of approximately 10 minutes. During the pre-training, one milk pellet was available at the end of the two goal arms as reward and mice were allowed to consume the reward from both arms. For spatial nonmatching- to-place testing, mice were assessed in a counterbalanced order and each trial consisted of a sample run and a choice run. On the sample run, the mice were forced either left or right by the presence of a door, according to a pseudorandom sequence (with equal numbers of left and right turns per session, and with not more than two consecutive turns in the same direction). A reward consisting of one milk pellet was available at the end of the arm. The time interval between the sample run and the choice run was approximately 15 seconds. The animal was rewarded for choosing the previously unvisited arm (that is, for alternating). Criterion point for a correct trial was that the whole animal (including the tip of the tail) entered the rewarded arm. Maze was cleaned between trials to avoid any potential odor cues. Each daily session consisted of 4 trials and mice were run one trial at a time with an ITI of approximately 10 minutes.

Open field. The open field consisted of a white PVC enclosed arena (70 x 70 x 30 cm) under uniform lightning conditions (20 LUX). The arena was delimited into two regions using the EthoVision software: an outer zone and an inner zone, a central square area of 35 x 35 cm equidistant from the walls. Mice were placed individually into one corner of the arena facing the sidewalls and were allowed to explore for 10 minutes. The time spent, velocity and total distance moved were recorded and video-tracked using EthoVision software.

Novel object recognition task. The object recognition task took place in the open field apparatus. Mice were individually habituated to the arena for two days. During the training session, two identical objects A1 and A2 were placed into the open field at 20 cm from the walls and the mouse was allowed to explore for 10 minutes. On the short-term memory (STM) testing trial, after an ITI of 5 minutes spent in the home cage, the animals were placed back into the open field, where one of the familiar objects was replaced by a novel object B, and allowed to explore freely for 10 minutes. The position of the novel object (left or right) was randomized between each mouse and each group tested. On the long-term memory (LTM) testing trial (24 hours after the STM testing trial), mice were allowed to explore the open field for 10 minutes in the presence of two objects: the familiar object A and a second novel object C. The novel object (B or C) was randomized in the STM or LTM sessions between each mouse and each group tested. All objects presented similar textures and sizes, but distinctive shapes and colors. Between trials, the objects were washed with 1% Anistel® solution to avoid the use of odor cues. The mice did not show any object preference before trials. Exploratory behavior was videotaped and video-tracked with the EthoVision software and it was measured *post hoc* using two stopwatches to record the time spent exploring the objects during the experimental sessions. A 20 seconds criterion of total exploration (or 10 minutes/session when the criterion was not reached) was used to score exploratory behavior. Object exploration was assessed only if the total time of exploration for each mouse was higher than 5 seconds in the training session. Exploration was scored whenever the mouse sniffed or touched the object while looking at it (i.e., when the distance between the nose and the object was less than 2 cm). Climbing onto the object (unless the mouse sniffed the object it had climbed on) did not qualify as exploration. To measure recognition memory, a discrimination index (DI) was calculated as the difference in exploration time between the novel and familiar objects, divided by the total time spent exploring both objects [(novel arm – familiar arm) / (novel arm + familiar arm)].

Spatial novelty preference in a Y-maze. Spatial novelty preference was assessed as described previously (Sanderson et al., 2009). Briefly, the spontaneous spatial novelty preference test was conducted using an 8 arm radial maze made from transparent Perspex with arms of 22 x 7 x 20 cm. The maze was placed into a room containing a variety of extra-maze cues. Mice were assigned two arms ("start arm" and "familiar arm") while the entrance to the third arm (the "novel arm" during the subsequent test phase) was blocked off with a black door. Allocation of arms (familiar and novel) to specific spatial locations was counterbalanced within each experimental group. During the exposure phase mice were allowed to explore the two arms for 5 minutes in the one trial exposure test or for 2 minutes five times, spaced by an ITI of 1 minute in the home cage, in the incremental training test. The mouse was then removed from the maze and returned to its home cage for a 1-minute interval between the exposure and test phases. During the test phase, mice were placed at the end of the start arm and allowed to explore all three arms for 2 minutes. An entry into an arm was defined by a mouse placing the forepaws inside an arm. Similarly, a mouse was considered to have left an arm if the forepaws were placed outside the arm. Exploratory behavior was videotaped and video-tracked with the EthoVision software and the number of entries and the time that mice spent in each arm were recorded manually. For the test phase, a discrimination index DI = [novel arm – familiar arm] / [novel arm + familiar arm] was calculated for both arm entries and time spent in arms.

Statistical analysis

All statistical analyses were performed using GraphPad Prism 6 (GraphPad Softwares) or SPSS (IBM Corp) softwares. Unless otherwise stated, parametric data were analyzed by *t*-test or one-way ANOVA followed by the Sidak, Holm's or Tukey *post hoc* analysis for comparisons of multiple samples. Non-parametric data were analyzed by the Mann-Whitney rank sum test or Kruskal-Wallis one-way analysis of variance on ranks followed by the Dunn *post hoc* analysis for comparisons of multiple samples. Probability distributions were compared using the Kolmogorov-Smirnov test. Statistical details of experiments can be found in the figure legends. P values <0.05 were considered statistically significant. Data are presented as mean ± SEM.

BIBLIOGRAPHY

Betzig, E., Patterson, G.H., Sougrat, R., Lindwasser, O.W., Olenych, S., Bonifacino, J.S., Davidson, M.W., Lippincott-Schwartz, J., and Hess, H.F. (2006). Imaging intracellular fluorescent proteins at nanometer resolution. Science *313*, 1642–1645.

Bloodgood, B.L., Sharma, N., Browne, H.A., Trepman, A.Z., and Greenberg, M.E. (2013). The activity-dependent transcription factor NPAS4 regulates domain-specific inhibition. Nature *503*, 121–125.

Brakebusch, C., Seidenbecher, C.I., Rauch, U., Matthies, H., Meyer, H., Krug, M., Böckers, T.M., Zhou, X., Kreutz, R., Montag, D., et al. (2002). Brevican-Deficient Mice Display Impaired Hippocampal CA1 Long-Term Potentiation but Show No Obvious Deficits in Learning and Memory Brevican-Deficient Mice Display Impaired Hippocampal CA1 Long-Term Potentiation but Show No Obvious Deficits in Learning an.

Brückner, G., Brauer, K., Härtig, W., Wolff, J.R., Rickmann, M.J., Derouiche, A., Delpech, B., Girard, N., Oertel, W.H., and Reichenbach, A. (1993). Perineuronal nets provide a polyanionic, glia-associated form of microenvironment around certain neurons in many parts of the rat brain. Glia *8*, 183–200.

Cardin, J.A., Carlén, M., Meletis, K., Knoblich, U., Zhang, F., Deisseroth, K., Tsai, L.-H., and Moore, C.I. (2009). Driving fast-spiking cells induces gamma rhythm and controls sensory responses. Nature *459*, 663–667.

Carstens, K.E., Phillips, M.L., Pozzo-Miller, L., Weinberg, R.J., and Dudek, S.M. (2016). Perineuronal Nets Suppress Plasticity of Excitatory Synapses on CA2 Pyramidal Neurons. J Neurosci *36*, 6312–6320.

Chang, M.C., Park, J.M., Pelkey, K.A., Grabenstatter, H.L., Xu, D., Linden, D.J., Sutula, T.P., McBain, C.J., and Worley, P.F. (2010). Narp regulates homeostatic scaling of excitatory synapses on parvalbumin-expressing interneurons. Nat Neurosci *13*, 1090–1097.

Clarke, L.E., and Barres, B.A. (2013). Emerging roles of astrocytes in neural circuit development. Nat Rev Neurosci *14*, 311–321.

Dani, A., Huang, B., Bergan, J., Dulac, C., and Zhuang, X. (2010). Superresolution imaging of chemical synapses in the brain. Neuron *68*, 843–856.

Deepa, S.S., Carulli, D., Galtrey, C., Rhodes, K., Fukuda, J., Mikami, T., Sugahara, K., and Fawcett, J.W. (2006). Composition of perineuronal net extracellular matrix in rat brain: a different disaccharide composition for the net-associated proteoglycans. J Biol Chem *281*, 17789–17800.

Dehorter, N., Ciceri, G., Bartolini, G., Lim, L., del Pino, I., and Marín, O. (2015). Tuning of fast-spiking interneuron properties by an activity-dependent transcriptional switch. Science *349*, 1216–1220.

Donato, F., Rompani, S.B., and Caroni, P. (2013). Parvalbumin-expressing basket-cell network plasticity induced by experience regulates adult learning. Nature *504*, 272–276.

Du, J., Zhang, L., Weiser, M., Rudy, B., and McBain, C.J. (1996). Developmental expression and functional characterization of the potassium-channel subunit Kv3.1b in parvalbumin-containing interneurons of the rat hippocampus. J Neurosci *16*, 506–518.

Frischknecht, R., Heine, M., Perrais, D., Seidenbecher, C.I., Choquet, D., and Gundelfinger, E.D. (2009). Brain extracellular matrix affects AMPA receptor lateral mobility and short-term synaptic plasticity. Nat Neurosci *12*, 897–904.

Frischknecht, R., Chang, K.-J., Rasband, M.N., and Seidenbecher, C.I. (2014). Neural ECM molecules in axonal and synaptic homeostatic plasticity. Prog Brain Res *214*, 81–100.

Froemke, R.C. (2015). Plasticity of cortical excitatory-inhibitory balance. Annu Rev Neurosci *38*, 195–219.

Fuchs, E.C., Zivkovic, A.R., Cunningham, M.O., Middleton, S., Lebeau, F.E.N., Bannerman, D.M., Rozov, A., Whittington, M.A., Traub, R.D., Rawlins, J.N.P., et al. (2007). Recruitment of parvalbumin-positive interneurons determines hippocampal function and associated behavior. Neuron *53*, 591–604.

Gogolla, N., Caroni, P., Lüthi, A., and Herry, C. (2009). Perineuronal nets protect fear memories from erasure. Science *325*, 1258–1261.

Goldberg, E.M., Clark, B.D., Zagha, E., Nahmani, M., Erisir, A., and Rudy, B. (2008). K+ channels at the axon initial segment dampen near-threshold excitability of neocortical fast-spiking GABAergic interneurons. Neuron *58*, 387–400.

Gu, S., Jin, L., Zhang, Y., Huang, Y., Zhang, F., Valdmanis, P.N., and Kay, M.A. (2012). The loop position of shRNAs and pre-miRNAs is critical for the accuracy of dicer processing in vivo. Cell *151*, 900–911.

Henley, J.M., and Wilkinson, K.A. (2016). Synaptic AMPA receptor composition in development, plasticity and disease. Nat Rev Neurosci *17*, 337–350.

Hensch, T.K., Fagiolini, M., Mataga, N., Stryker, M.P., Baekkeskov, S., and Kash, S.F. (1998). Local GABA circuit control of experience-dependent plasticity in developing visual cortex. Science *282*, 1504–1508.

Hippenmeyer, S., Vrieseling, E., Sigrist, M., Portmann, T., Laengle, C., Ladle, D.R., and Arber, S. (2005). A developmental switch in the response of DRG neurons to ETS transcription factor signaling. PLoS Biol *3*, e159.

Hockfield, S., and McKay, R.D. (1983). A surface antigen expressed by a subset of neurons in the vertebrate central nervous system. Proc Natl Acad Sci U S A *80*, 5758–5761.

Hu, H., Gan, J., and Jonas, P. (2014). Interneurons. Fast-spiking, parvalbumin$^+$ GABAergic interneurons: from cellular design to microcircuit function. Science *345*, 1255263.

Karson, M.A., Tang, A.-H., Milner, T.A., and Alger, B.E. (2009). Synaptic cross talk between perisomatic-targeting interneuron classes expressing cholecystokinin and parvalbumin in hippocampus. J Neurosci *29*, 4140–4154.

Katona, I., Sperlágh, B., Sík, A., Käfalvi, A., Vizi, E.S., Mackie, K., and Freund, T.F. (1999). Presynaptically located CB1 cannabinoid receptors regulate GABA release from axon terminals of specific hippocampal interneurons. J Neurosci *19*, 4544–4558.

Kitamura, T., Sun, C., Martin, J., Kitch, L.J., Schnitzer, M.J., and Tonegawa, S. (2015). Entorhinal Cortical Ocean Cells Encode Specific Contexts and Drive Context-Specific Fear Memory. Neuron *87*, 1317–1331.

Klausberger, T., and Somogyi, P. (2008). Neuronal diversity and temporal dynamics: the unity of hippocampal circuit operations. Science *321*, 53–57.

Kochlamazashvili, G., Henneberger, C., Bukalo, O., Dvoretskova, E., Senkov, O., Lievens, P.M.-J., Westenbroek, R., Engel, A.K., Catterall, W.A., Rusakov, D.A., et al. (2010). The extracellular matrix molecule hyaluronic acid regulates hippocampal synaptic plasticity by modulating postsynaptic L-type Ca(2+) channels. Neuron *67*, 116–128.

Lagler, M., Ozdemir, A.T., Lagoun, S., Malagon-Vina, H., Borhegyi, Z., Hauer, R., Jelem, A., and Klausberger, T. (2016). Divisions of Identified Parvalbumin-Expressing Basket Cells during Working Memory-Guided Decision Making. Neuron *91*, 1390–1401.

Lander, C., Kind, P., Maleski, M., and Hockfield, S. (1997). A family of activity-dependent neuronal cell-surface chondroitin sulfate proteoglycans in cat visual cortex. J Neurosci *17*, 1928–1939.

Matta, J.A., Pelkey, K.A., Craig, M.T., Chittajallu, R., Jeffries, B.W., and McBain, C.J. (2013). Developmental origin dictates interneuron AMPA and NMDA receptor subunit composition and plasticity. Nat Neurosci *16*, 1032–1041.

Nabel, E.M., and Morishita, H. (2013). Regulating critical period plasticity: insight from the visual system to fear circuitry for therapeutic interventions. Frontiers in Psychiatry *4*, 146.

Okaty, B.W., Miller, M.N., Sugino, K., Hempel, C.M., and Nelson, S.B. (2009). Transcriptional and electrophysiological maturation of neocortical fast-spiking GABAergic interneurons. J Neurosci *29*, 7040–7052.

Pizzorusso, T., Medini, P., Berardi, N., Chierzi, S., Fawcett, J.W., and Maffei, L. (2002). Reactivation of ocular dominance plasticity in the adult visual cortex. Science *298*, 1248–1251.

Platonova, E., Winterflood, C.M., and Ewers, H. (2015). A simple method for GFP- and RFP-based dual color single-molecule localization microscopy. ACS Chem Biol *10*, 1411–1416.

Reisel, D., Bannerman, D.M., Schmitt, W.B., Deacon, R.M.J., Flint, J., Borchardt, T., Seeburg, P.H., and Rawlins, J.N.P. (2002). Spatial memory dissociations in mice lacking GluR1. Nat Neurosci *5*, 868–873.

Sanderson, D.J., Gray, A., Simon, A., Taylor, A.M., Deacon, R.M.J., Seeburg, P.H., Sprengel, R., Good, M.A., Rawlins, J.N.P., and Bannerman, D.M. (2007). Deletion of glutamate receptor-A (GluR-A) AMPA receptor subunits impairs one-trial spatial memory. Behav Neurosci *121*, 559–569.

Sanderson, D.J., Good, M.A., Skelton, K., Sprengel, R., Seeburg, P.H., Rawlins, J.N.P., and Bannerman, D.M. (2009). Enhanced long-term and impaired short-term spatial memory in GluA1 AMPA receptor subunit knockout mice: evidence for a dual-process memory model. Learn Mem *16*, 379–386.

Schweizer, M., Streit, W.J., and Müller, C.M. (1993). Postnatal development and localization of an N-acetylgalactosamine containing glycoconjugate associated with nonpyramidal neurons in cat visual cortex. J Comp Neurol *329*, 313–327.

Seidenbecher, C.I., Richter, K., Rauch, U., Fässler, R., Garner, C.C., and Gundelfinger, E.D. (1995). Brevican, a chondroitin sulfate proteoglycan of rat brain, occurs as secreted and cell surface glycosylphosphatidylinositol-anchored isoforms. J Biol Chem *270*, 27206–27212.

Seidenbecher, C.I., Smalla, K.H., Fischer, N., Gundelfinger, E.D., and Kreutz, M.R. (2002). Brevican isoforms associate with neural membranes. J Neurochem *83*, 738–746.

Sohal, V.S., Zhang, F., Yizhar, O., and Deisseroth, K. (2009). Parvalbumin neurons and gamma rhythms enhance cortical circuit performance. Nature *459*, 698–702.

Takesian, A.E., and Hensch, T.K. (2013). Balancing plasticity/stability across brain development. Prog Brain Res *207*, 3–34.

Tsien, R.Y. (2013). Very long-term memories may be stored in the pattern of holes in the perineuronal net. Proc Natl Acad Sci U S A *110*, 12456–12461.

Turrigiano, G. (2012). Homeostatic synaptic plasticity: local and global mechanisms for stabilizing neuronal function. Cold Spring Harb Perspect Biol *4*, a005736.

Valenzuela, J.C., Heise, C., Franken, G., Singh, J., Schweitzer, B., Seidenbecher, C.I., and Frischknecht, R. (2014). Hyaluronan-based extracellular matrix under conditions of homeostatic plasticity. Philos Trans R Soc Lond, B, Biol Sci *369*, 20130606.

Wilson, N.R., Runyan, C.A., Wang, F.L., and Sur, M. (2012). Division and subtraction by distinct cortical inhibitory networks in vivo. Nature *488*, 343–348.

Winterflood, C.M., Platonova, E., Albrecht, D., and Ewers, H. (2015). Dual-color 3D superresolution microscopy by combined spectral-demixing and biplane imaging. Biophys J *109*, 3–6.

de Wit, J., O'Sullivan, M.L., Savas, J.N., Condomitti, G., Caccese, M.C., Vennekens, K.M., Yates, J.R., and Ghosh, A. (2013). Unbiased discovery of glypican as a receptor for LRRTM4 in regulating excitatory synapse development. Neuron *79*, 696–711.

Xue, M., Atallah, B.V., and Scanziani, M. (2014). Equalizing excitation-inhibition ratios across visual cortical neurons. Nature *511*, 596–600.

Yazaki-Sugiyama, Y., Kang, S., Câteau, H., Fukai, T., and Hensch, T.K. (2009). Bidirectional plasticity in fast-spiking GABA circuits by visual experience. Nature *462*, 218–221.

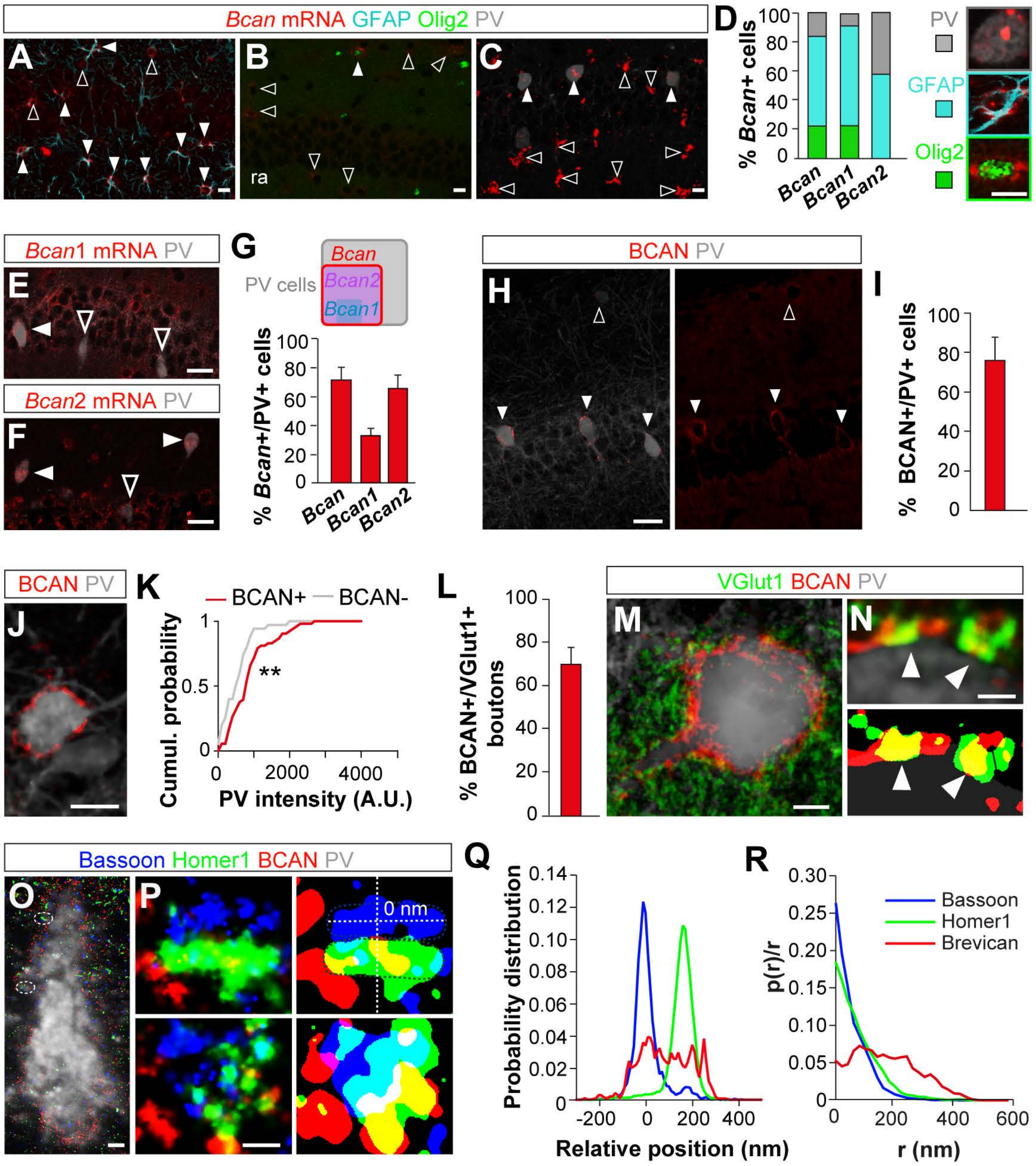

Figure 1

Favuzzi et al.

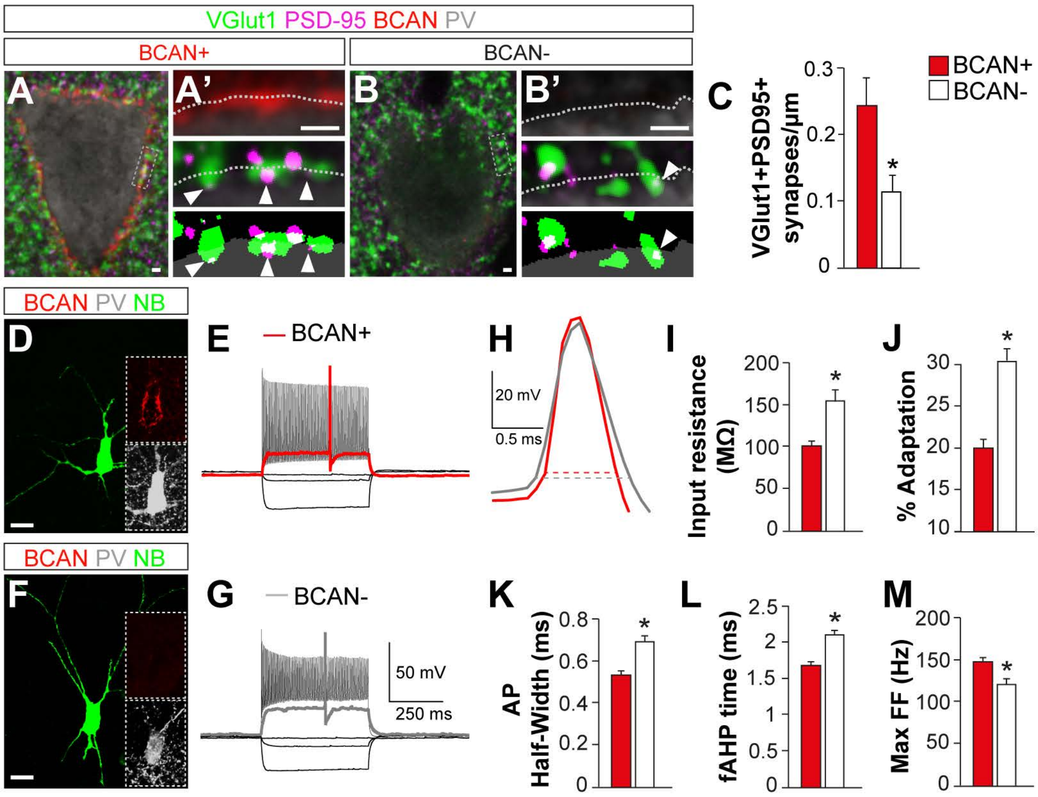

Figure 2

Favuzzi et al.

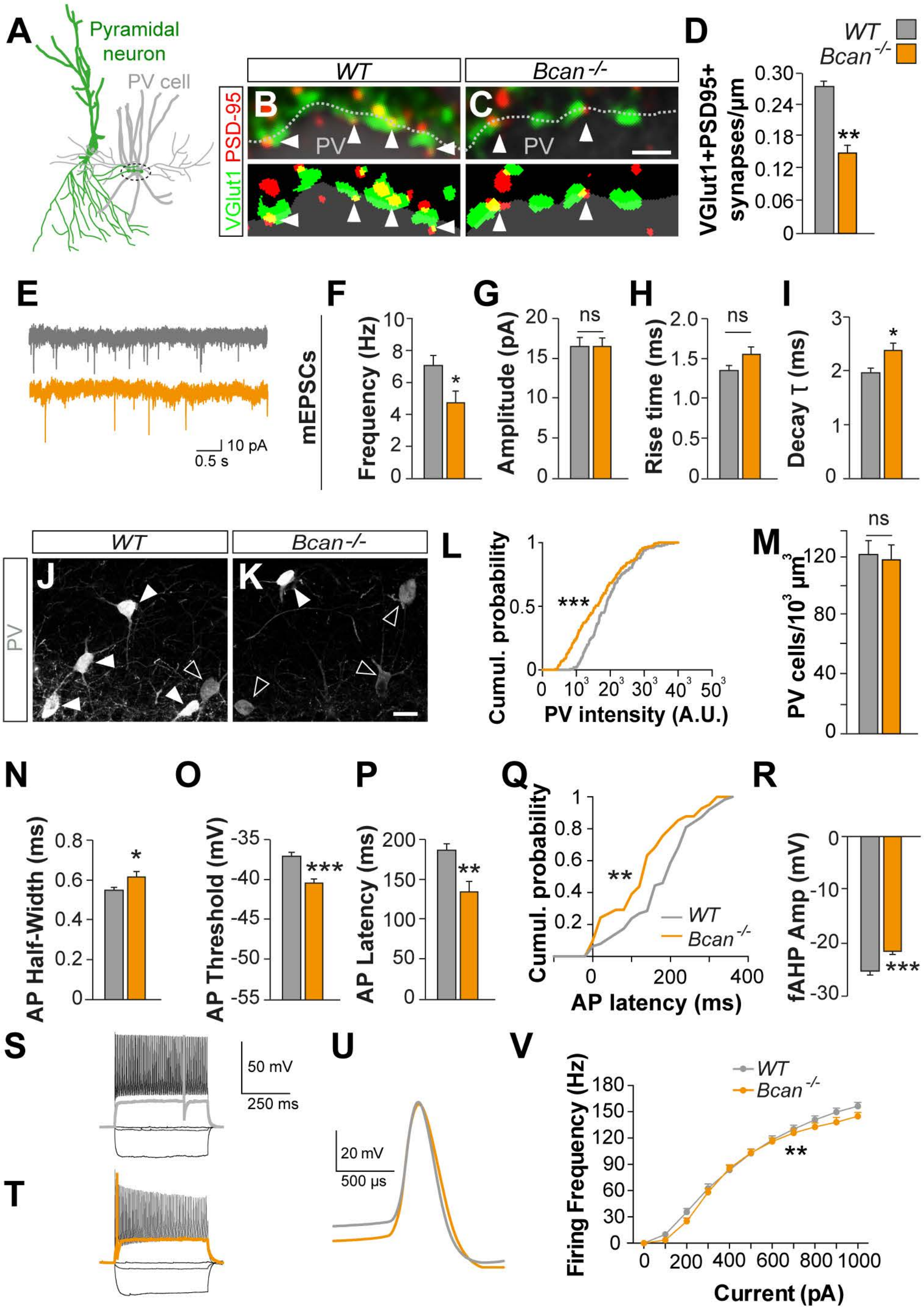

Figure 3

Favuzzi et al.

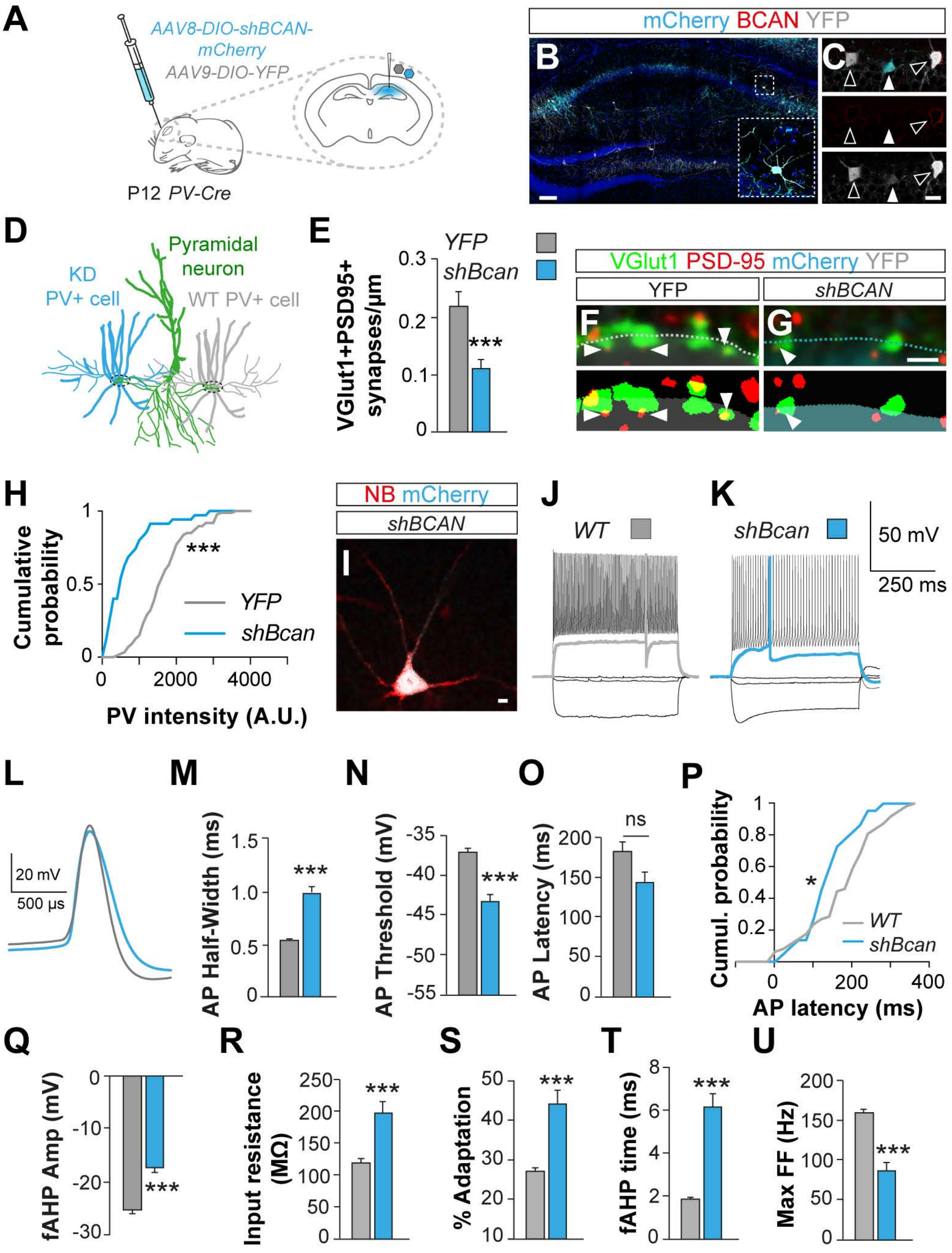

Figure 4

Favuzzi et al.

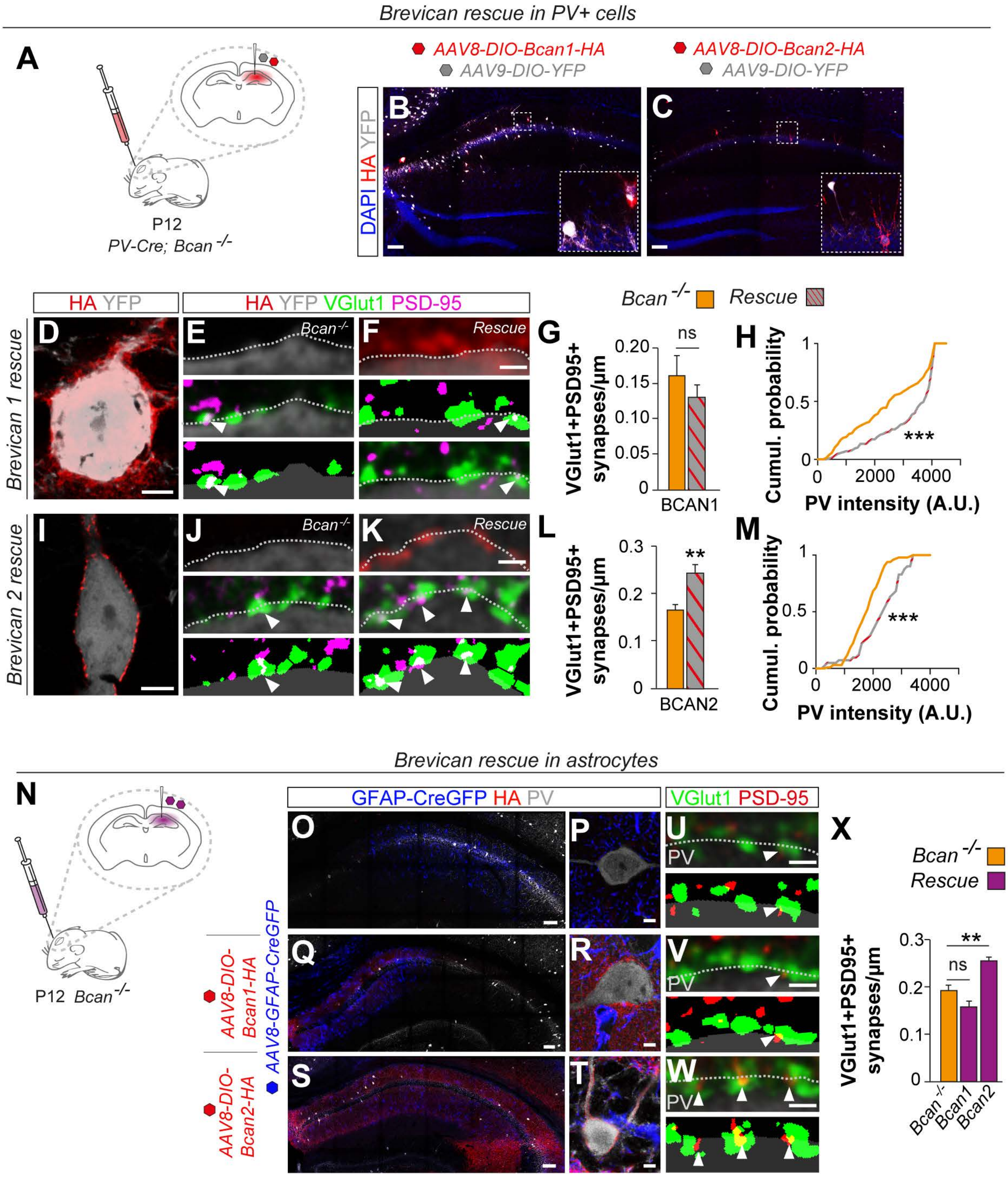

Figure 5

Favuzzi et al.

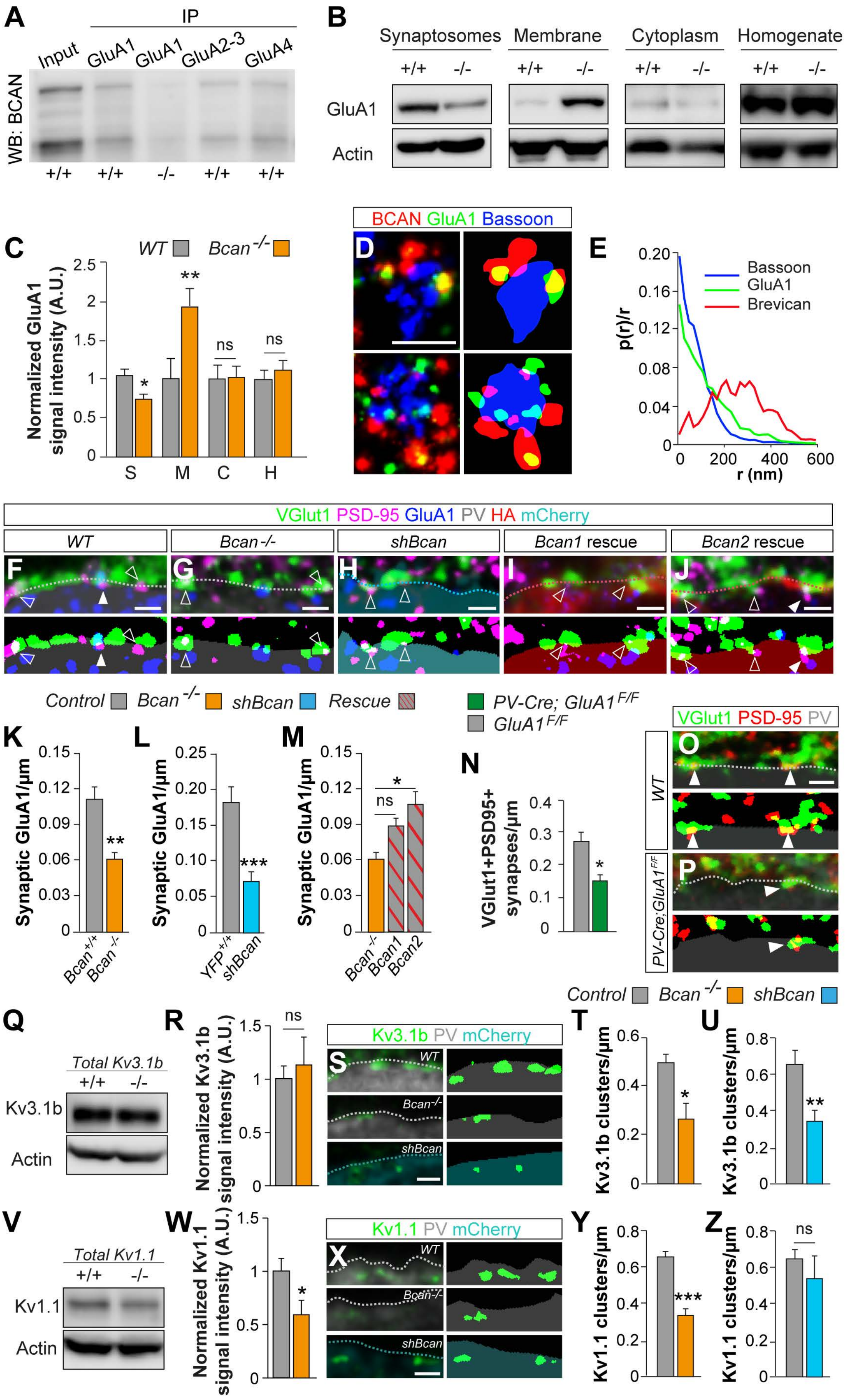

Figure 6

Favuzzi et al.

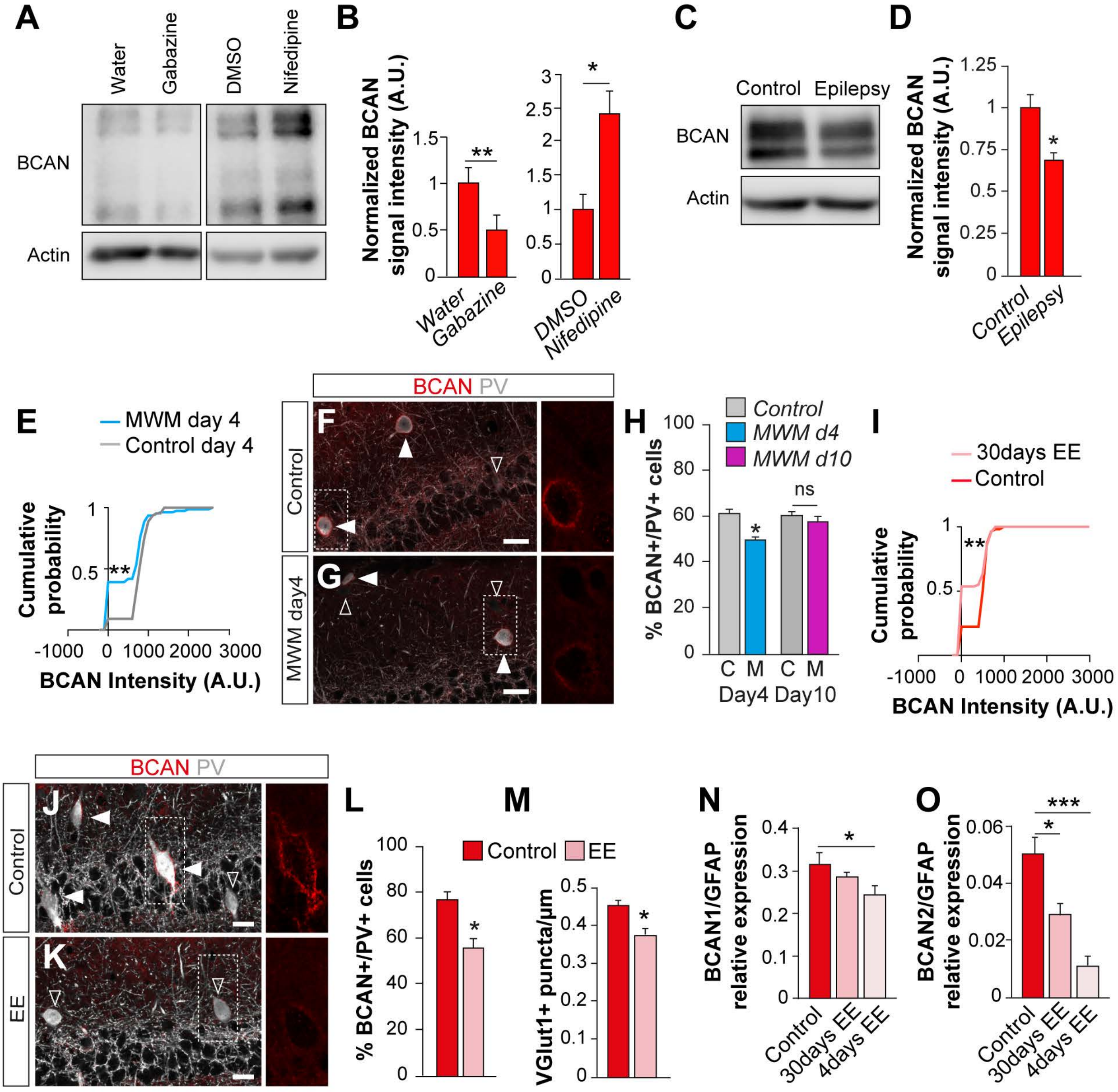

Figure 7

Favuzzi et al.

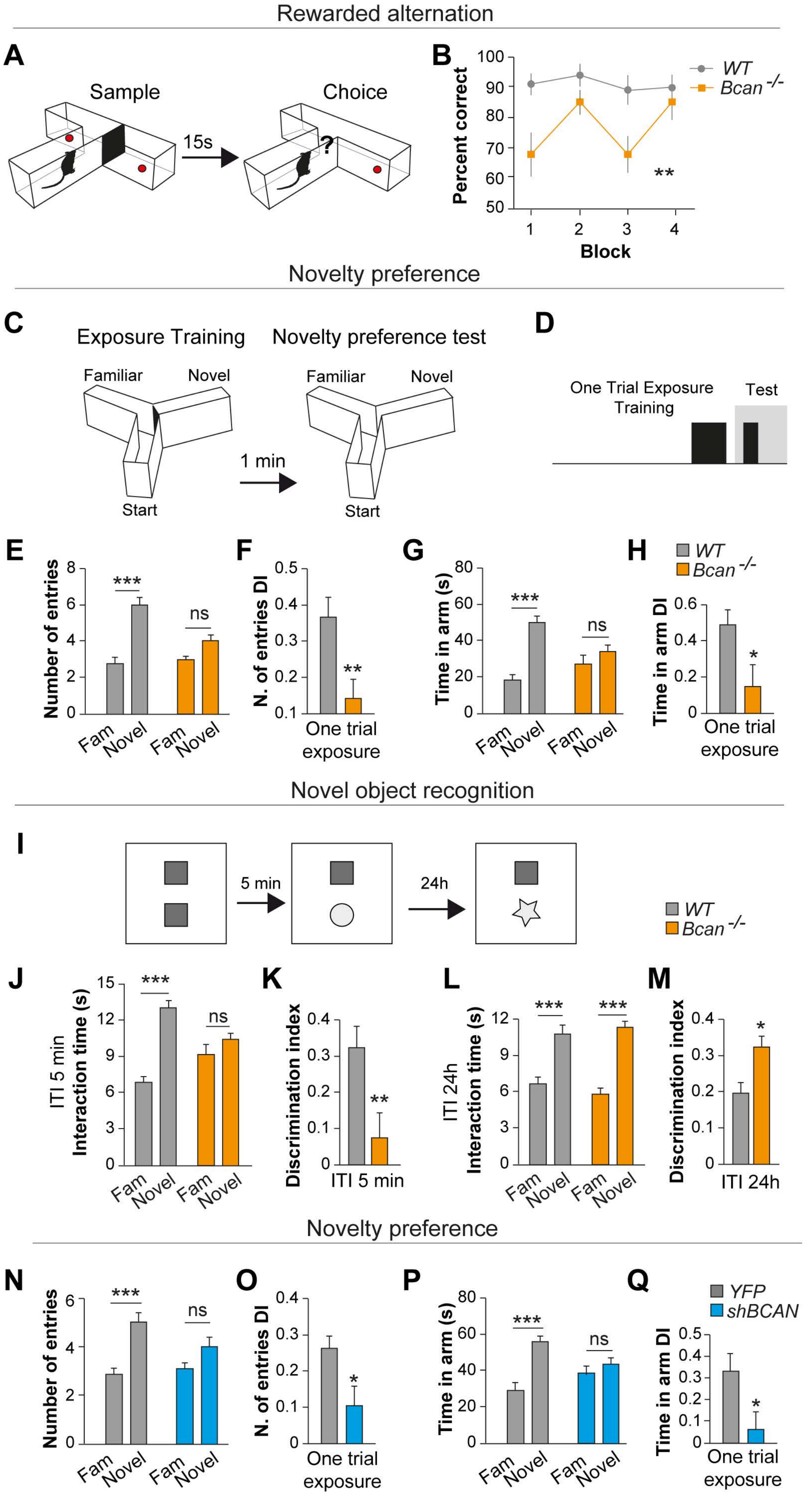

Figure 8

Favuzzi et al.

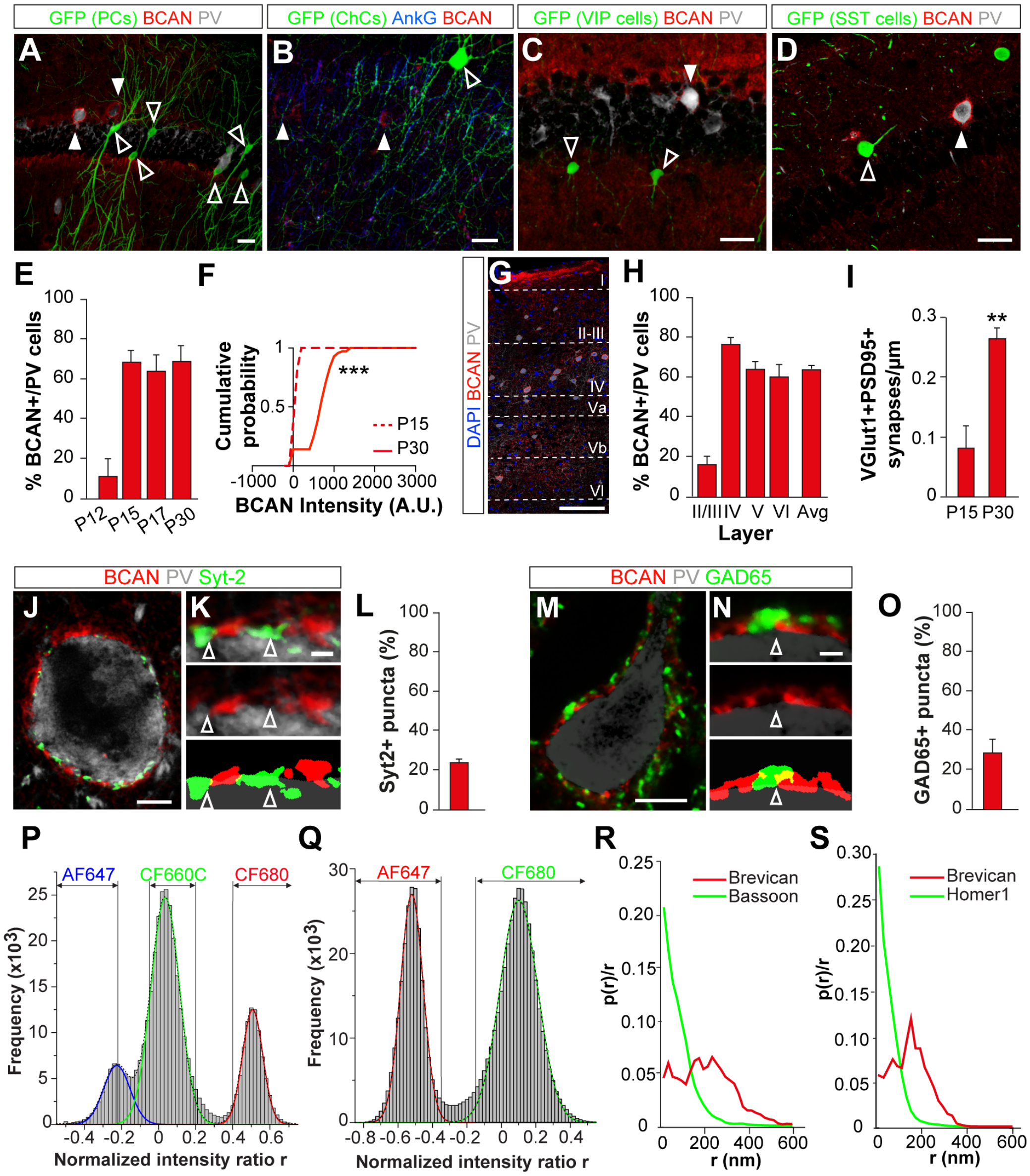

Figure S1

Favuzzi et al.

SUPPLEMENTAL FIGURES

Figure S1. Expression and localization of Brevican in the cerebral cortex, related to Figure 1

(A-D) Representative images showing the absence of Brevican sheath surrounding pyramidal cells or interneuron subtypes (empty arrowheads) other than PV+ basket cells (arrowheads). PCs: GFP-electroporated pyramidal cells, ChCs: chandelier cells in *Nkx2.1CreERT2;RCE*, VIP cells: *VIP-Cre; RCE*, SST cells: *GIN* mice.

(E) Percentage of PV+ interneurons enwrapped by Brevican protein at different postnatal developmental stages in the hippocampus (n = 3 mice). P30 data are the same as in Figure 1I.

(F) Cumulative probability plot comparing Brevican fluorescence intensity levels at P15 (n = 55 cells, 3 mice) and P30 (n = 142 cells, 4 mice) mice; Kolmogorov-Smirnov test.

(G and H) Representative image (G) and percentage (H) of PV+ interneurons enwrapped by Brevican protein in the somatosensory cortex (n = 4 mice).

(I) Density of VGlut1+PSD95+ synapses contacting the soma of PV+ cells at P15 (n = 7 mice) and P30 (n = 6 mice); Mann-Whitney test. P15 and P30 data are the same as the controls in Figure S3E and Figure 3D, respectively.

(J-O) Representative images and percentage of Syt2+ (J-L, n = 4 mice) and GAD65+ (M-O, n = 3 mice) inhibitory terminals contacting the soma of PV+BCAN+ cells.

(P and Q) Histograms of normalized intensity ratios and dye separation for a three-color STORM experiment using Bassoon-AF647, Homer-CF660 and Brevican-CF680 (P) and for a two-color STORM experiment using Brevican-AF647 and Bassoon-CF680 (Q).

(R and S) Radial (lateral) distribution of Brevican and Bassoon (R) or Homer1 (S). Analysis of 51 (R) and 41 (S) face-view synapses from 6 experiments. Scale bars equal 20 μm (A-D), 100 μm (G), 5 μm (J, M), 1 μm (K, N).

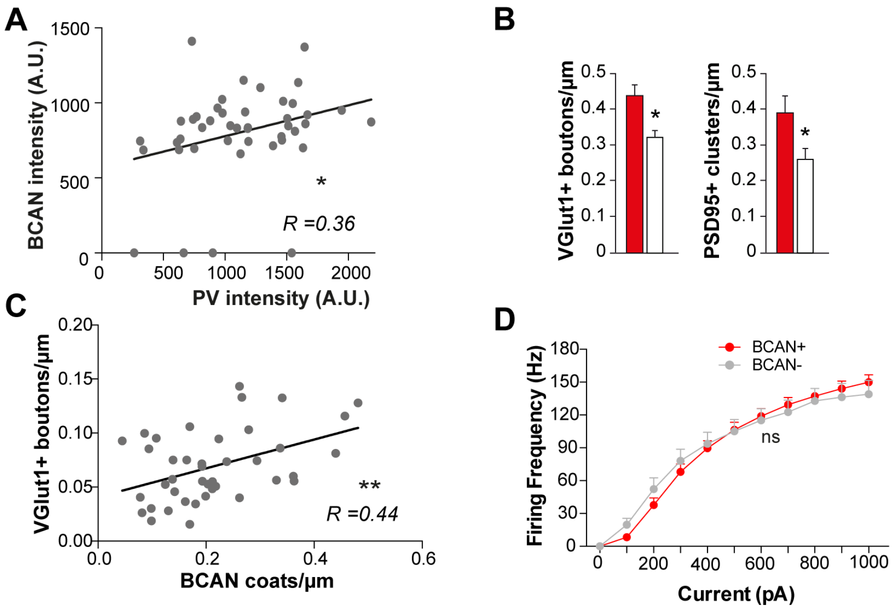

Figure S2

Favuzzi et al.

Figure S2. Characterization of Brevican+ and Brevican- cells, related to Figure 2

(A) Correlation between the PV and Brevican protein intensities in PV+ cells (Spearman correlation, n = 44 cells, 3 mice).

(B) Density of VGlut1+ boutons (n = 7 mice) and PSD95+ clusters (n = 9 mice) contacting the soma of BCAN+ and BCAN- PV cells. Student t-test.

(C) Correlation between the number of Brevican “coats” (see supplemental experimental procedures for details) and the number of VGlut1+ inputs contacting PV+ interneurons (Pearson correlation, n = 41 cells, 3 mice).

(D) I/O curves showing the spike frequency of BCAN+ (n = 22 cells, 9 mice) and BCAN- (n = 13 cells, 9 mice) PV+ cells in response to current injections (left Y-axis, solid lines). Note that the input-output curve was similar between the two populations of basket PV+ cells. Two-way ANOVA, F (1, 346) = 0.0170.

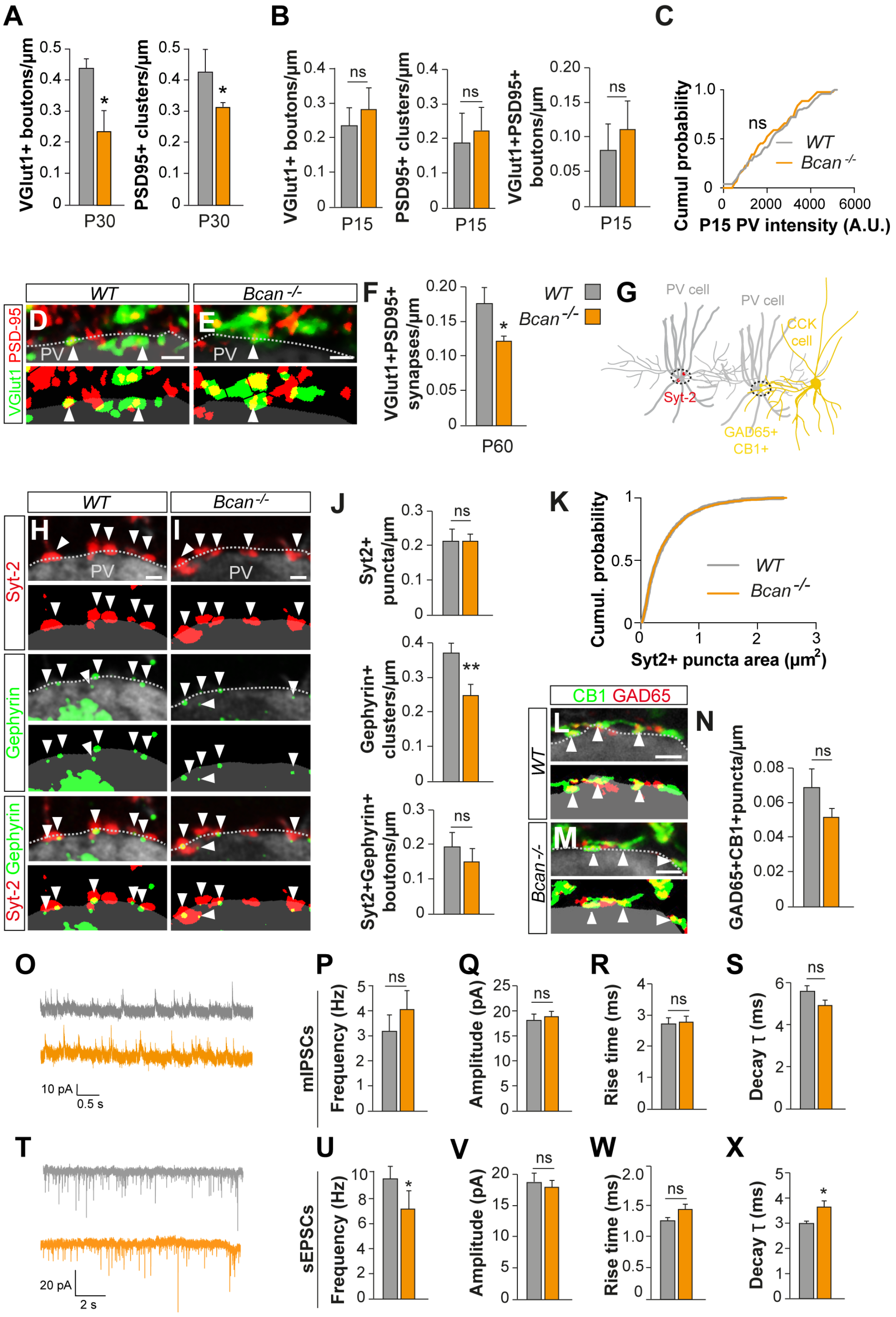

Figure S3

Favuzzi et al.

Figure S3. Effect of Brevican deletion on the wiring of PV+ interneurons, related to Figure 3

(A) Density of VGlut1+ boutons (n = 6 WT, 4 *Bcan*$^{-/-}$) and PSD95+ clusters (n = 7 WT, 7 *Bcan*$^{-/-}$) contacting the soma of PV+ cells at P30.

(B) Density of VGlut1+ boutons, PSD95+ clusters and VGlut1+PSD95+ synapses contacting the soma of PV+ cells in P15 wild type (WT, n = 7 mice) and *Bcan*$^{-/-}$ (n = 7 mice) mice.

(C) Cumulative probability plots comparing PV fluorescence intensity levels in P15 wild type (WT, n = 75 cells, 8 mice) and *Bcan*$^{-/-}$ (n = 44 cells, 3 mice) mice; ns: no significant difference.

(D-F) Representative images and thresholded binary images (D and E) illustrating VGlut1+PSD95+ synapses contacting the soma of PV+ cells, and synaptic density (F), in WT (n = 6 mice) and *Bcan*$^{-/-}$ (n = 8 mice) mice at P60.

(G) Schematic drawing highlighting the synapses analyzed in the following experiments.

(H-J) Representative images, thresholded binary images (H and I) and synaptic density (J). Images illustrate Syt2+ boutons (n= 5 WT, 4 *Bcan*$^{-/-}$), Gephyrin+ clusters (n = 12 WT, 11 *Bcan*$^{-/-}$) and Syt2+Gephyrin+ synapses (n = 5 WT, 4 *Bcan*$^{-/-}$) contacting the soma of PV+ cells.

(K) Cumulative probability plots comparing the size of Syt2 puncta in wild type (WT, n = 61 cells, 6 mice) and *Bcan*$^{-/-}$ (n = 82 cells, 4 mice) mice.

(L-N) Representative images and thresholded binary images (L and M) illustrating CB1+GAD65+ boutons contacting the soma of PV+ interneurons, and synaptic density (N) in WT (n = 5 mice) and *Bcan*$^{-/-}$ (n = 6 mice) mice .

(O-S) Representative traces, frequency, amplitude, rise and decay time of mIPSCs in WT (n = 11 cells, 4 mice) and *Bcan*$^{-/-}$ PV+ cells (n = 16 cells, 3 mice).

(T-X) Representative traces, frequency, amplitude, rise and decay time of sEPSCs in WT (n = 11 cells, 1 mouse) and *Bcan*$^{-/-}$ PV+ cells (n = 10 cells, 2 mice).

Student t-test (A, F, N, R, S, V, W, PSD95+ clusters in C, and Gephyrin+ clusters in J), Mann-Whitney test for (J, P, Q, U, X and VGlut1+ boutons in C). Kolmogorov-Smirnov test (B and K). Scale bars equal 1 μm (D, E, H, I), 2 μm (L, M).

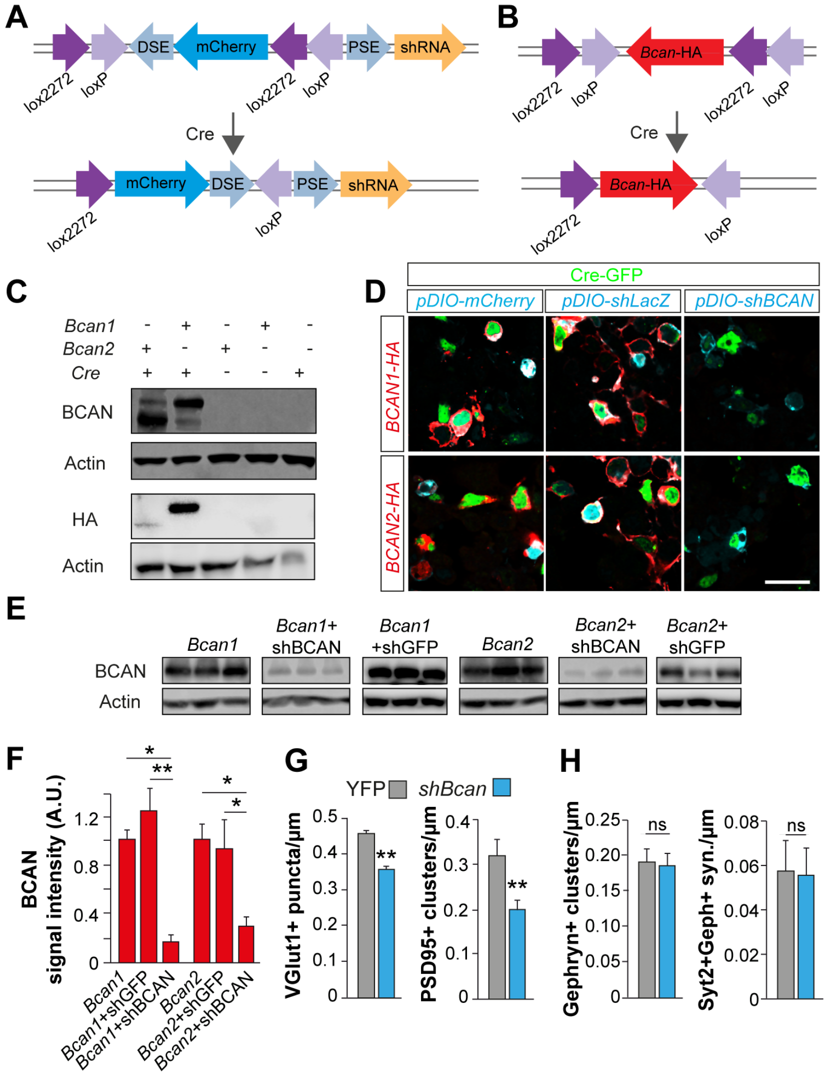

Figure S4
Favuzzi et al.

Figure S4. Strategy to knockdown Brevican in PV+ interneurons, related to Figure 4

(A and B) Diagram of the AAV cre-dependent constructs expressing *mCherry* and *shBcan* (A), or Brevican isoforms tagged with HA (B).

(C) Representative immunoblots from HEK293T cells co-transfected with *Cre-GFP* and *Brevican1-HA* or *Brevican2-HA* (n = 2 independent wells).

(D-F) Representative immunocytochemistry images (D) and immunoblots (E and F) illustrating downregulated Brevican expression upon co-transfection with plasmids expressing *shRNA* for Brevican (shBCAN). Cells were co-transfected with *Cre-GFP*, *shBrevican*, and *Bcan1-HA* or *Bcan2-HA*; n = 6 independent wells except *Bcan1*+shGFP and *Bcan1*+shBCAN where n = 9. Kruskal-Wallis test for *Bcan1* and one-way ANOVA for *Bcan2*. Scale bar 20 μm.

(G) Density of VGlut1+ boutons (n = 67 WT cells and 45 Brevican KD cells, from 5 mice) and PSD95+ clusters (n = 22 WT cells and 23 Brevican KD cells, from 3 mice) contacting the soma of PV+ cells. Student t-test.

(H) Density of Gephyrin+ clusters and Syt2+Gephyrin+ synapses (n = 28 WT cells and 25 Brevican KD cells, from 3 mice) contacting the soma of PV+ cells. Mann-Whitney test.

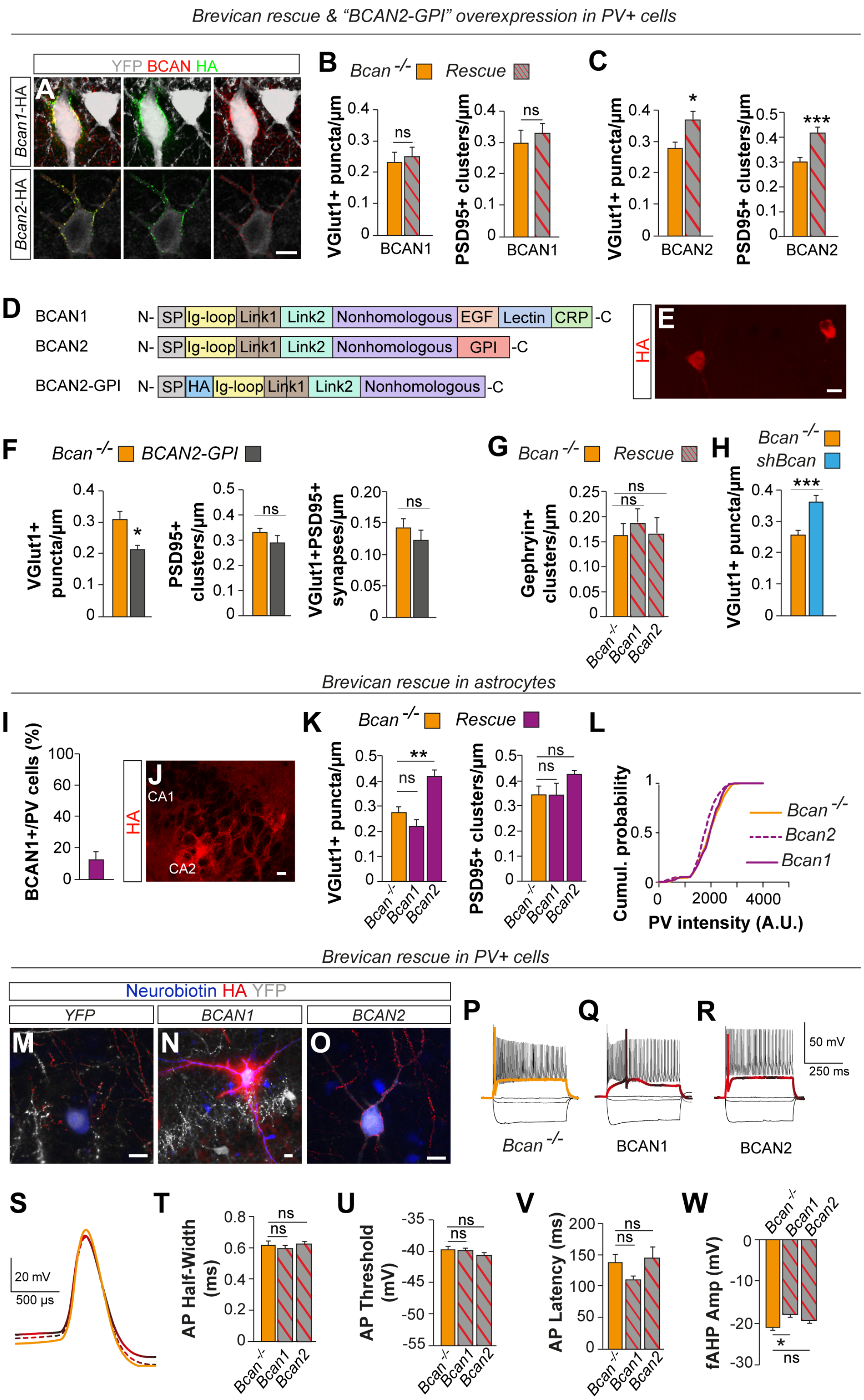

Figure S5

Favuzzi et al.

Figure S5. Overexpression of Brevican in PV+ interneurons and astrocytes, related to Figure 5

(A) Representative images of PV+ interneurons infected *in vivo* with AAVs expressing *Brevican1-HA* or *Brevican2-HA* and immunostained with BCAN antibody.

(B) Density of VGlut1+ boutons (n = 25 *Bcan*$^{-/-}$cells and 23 BCAN1 rescued cells, from 5 mice) and PSD95+ clusters (n = 40 WT cells and 40 BCAN1 rescued cells, from 5 mice) contacting the soma of PV+ cells.

(C) Density of VGlut1+ boutons (n = 24 *Bcan*$^{-/-}$cells and 23 BCAN2 rescued cells, from 6 mice) and PSD95+ clusters (n = 50 WT cells and 34 BCAN2 rescued cells, from 5 mice) contacting the soma of PV+ cells.

(D) Functional protein domains in BCAN1 and BCAN2 sequences and design of a BCAN2 mutant that lacks the GPI-anchor (BCAN2-GPI).

(E) Representative image showing how BCAN2-GPI is retained in the cytoplasm of PV+ cells.

(F) Density of VGlut1+ boutons, PSD95+ clusters and VGlut1+PSD95+ synapses (n = 30 *Bcan*$^{-/-}$, 21 BCAN2-GPI expressing cells, 4 mice) contacting the soma of PV+ cells.

(G) Density of Gephyrin+ clusters in *Bcan*$^{-/-}$ (n = 19 cells, 5 animals), BCAN1 (n= 13 cells, 4 animals) and BCAN2 (n = 17 cells, 3 animals) PV+ cells.

(H) Comparison between the density of VGlut1+ boutons in Brevican KD cells (45 cells, from Figure S4G) and *Bcan*$^{-/-}$ cells (49 cells, pool of data from Figure 5B and S5C).

(I) Percentage of PV+ cells that are surrounded by BCAN1-HA secreted from astrocytes infected with GFAP-CreGFP and BCAN1-HA expressing viruses.

(J) Representative image showing CA2 pyramidal neurons surrounded by BCAN1 secreted from astrocytes that had been infected with GFAP-CreGFP and BCAN1-HA Cre-dependent virus.

(K) Density of VGlut1+ boutons and PSD95+ clusters contacting the soma of PV+ cells in *Bcan*$^{-/-}$ mice infected with the control virus only (GFAP-CreGFP, n = 8 for VGlut1+ boutons and 6 mice for PSD95+ clusters) or together with BCAN1 (n = 4 mice) or BCAN2 (n = 3 mice for VGlut1+ boutons and 6 mice for PSD95+ clusters) expressing virus.

(L) Cumulative probability plots comparing PV fluorescence intensity levels in *Bcan*$^{-/-}$ mice in which astrocytes had been infected with the control virus only (GFAP-CreGFP, n = 360 cells, 6 mice) or together with BCAN1 (n = 202 cells, 4 mice) or BCAN2 (n = 227 cells, 3 mice) expressing virus. Note that neither BCAN1 nor BCAN2 were able to rescue the PV level, however the PV level in mice that overexpressed *Bcan2* in astrocytes was even lower than in *Bcan*$^{-/-}$ mice, Kolmogorov-Smirnov test ($p<0.0001$) whereas no significant differences were observed between *Bcan1* and *Bcan*$^{-/-}$ mice, Kolmogorov-Smirnov test ($p>0.05$).

(M-R) Representative images (M-O) and firing traces (P-R) for *Bcan*$^{-/-}$ (same as in Figure 3O), BCAN1 and BCAN2 overexpressing PV+ cells. (S) are insets from (P-R) illustrating the similar spike shape of *Bcan*$^{-/-}$, BCAN1 and BCAN2 rescued cells.

(T-W) Intrinsic electrophysiological properties comparing *Bcan*$^{-/-}$ (n = 53 cells, 13 mice), BCAN1 (n = 13 cells, 4 mice) and BCAN2 (n = 32 cells, 5 mice) overexpressing PV+ cells. Note that *Bcan*$^{-/-}$ cells used for comparison were a pool of the cells shown in Figure 3 and YFP+HA- cells from the injected mice. Mann-Whitney test (B, C, H, VGlut1+PSD95+ synapses in F), one-way ANOVA (G, K, U, V, W), Student t-test (F, VGlut+ boutons and PSD95+ clusters), Kolmogorov-Smirnov test (L), Kruskal–Wallis test (T). Scale bars equal 10 μm (A, E, J, M, N, O).

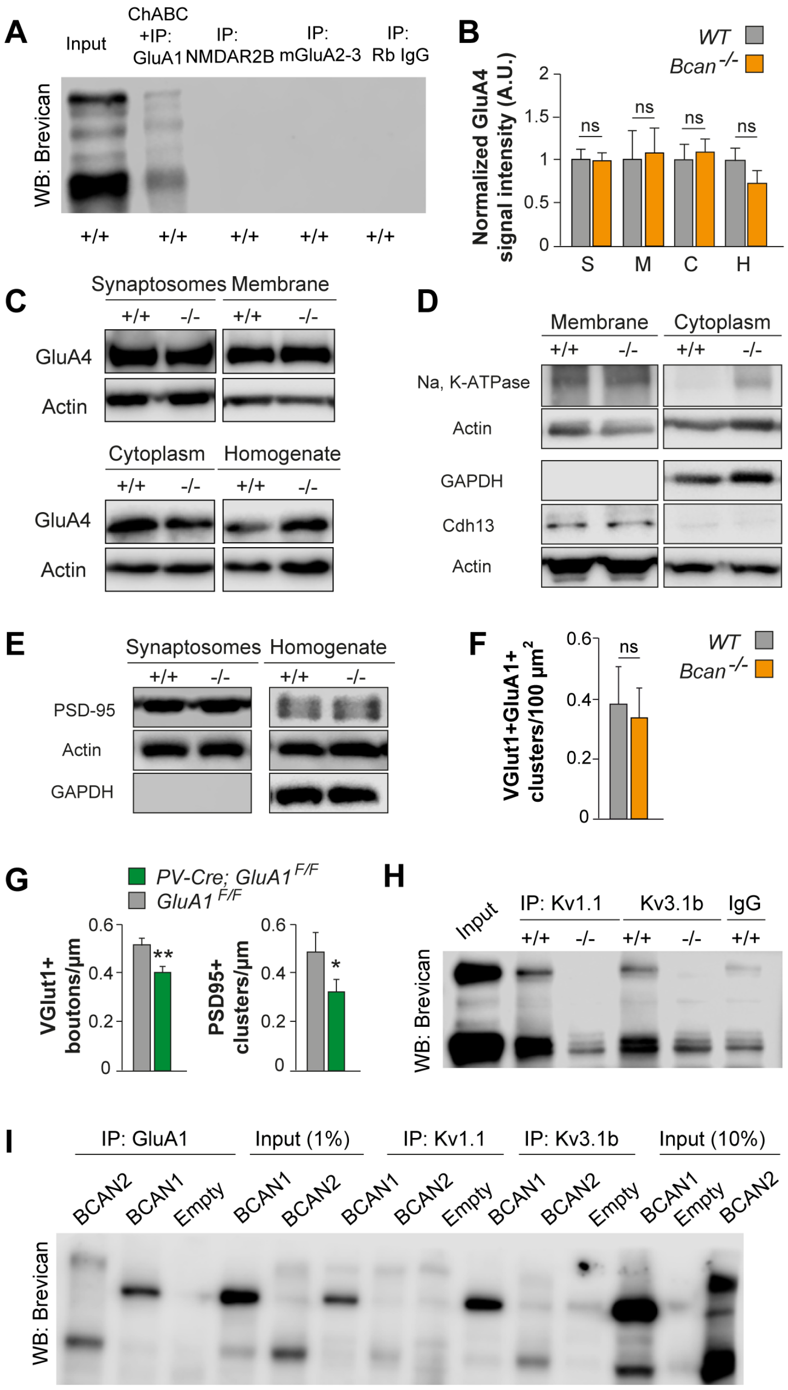

Figure S6

Favuzzi et al.

Figure S6. Interactions of Brevican with AMPA and potassium channels, related to Figure 6

(A) Representative immunoblot illustrating that pull-down of GluA1 from wild type hippocampal lysates previously digested with ChABC co-immunoprecipitates Brevican, showing that BCAN-GluA1 interactions is independent of the chondroitin sulfate chains. Note that pull-down of NMDA2B, mGluA2-3 or control IgG fails to co-immunoprecipitate Brevican (n = 2 Co-IP independent experiments).

(B and C) Quantification (B) and representative immunoblots (C) of GluA4 protein in the indicated cell fractions (n = 7-11 mice per genotype).

(D and E) Immunoblots of the fractionation controls showing enrichment of GAPDH in cytoplasmic fractions, of Na,K-ATPase and Cadherin13 in membrane fractions, and of PSD95 in synaptosomes.

(F) Density of GluA1+VGlut1+ clusters in the stratum radiatum of the hippocampus, a region largely populated by pyramidal cell dendrites, in WT (n = 3 mice) and *Bcan*$^{-/-}$ (n = 3 mice) mice. The similar density of GluA1+VGlut1+ clusters suggests a PV-specific deficit in GluA1 synaptic delivery.

(G) Density of VGlut1+ boutons and PSD95+ clusters contacting the soma of PV+ cells in *PV-Cre; GluA1* conditional mutants (n = 10 mice) compared to controls (n = 6 mice).

(H) Representative immunoblots illustrating that pull-down of Kv1.1 and Kv3.1b from WT hippocampal lysates co-immunoprecipitate Brevican (n = 2 mice). Note that although a non-specific band is detected, the difference in its intensity indicates that Kv1.1 and Kv3.1b fail to co-immunoprecipitate Brevican in *Bcan*$^{-/-}$ hippocampal lysates.

(I) Representative immunoblots illustrating that pull-down of GluA1, Kv1.1 and Kv3.1b from *Bcan*$^{-/-}$ hippocampal lysates co-immunoprecipitate BCAN1 and BCAN2 from transfected HEK cells (n = 1 Co-IP experiment from 2 independent transfections.

Student t-test (B) and Mann-Whitney test (F and G).

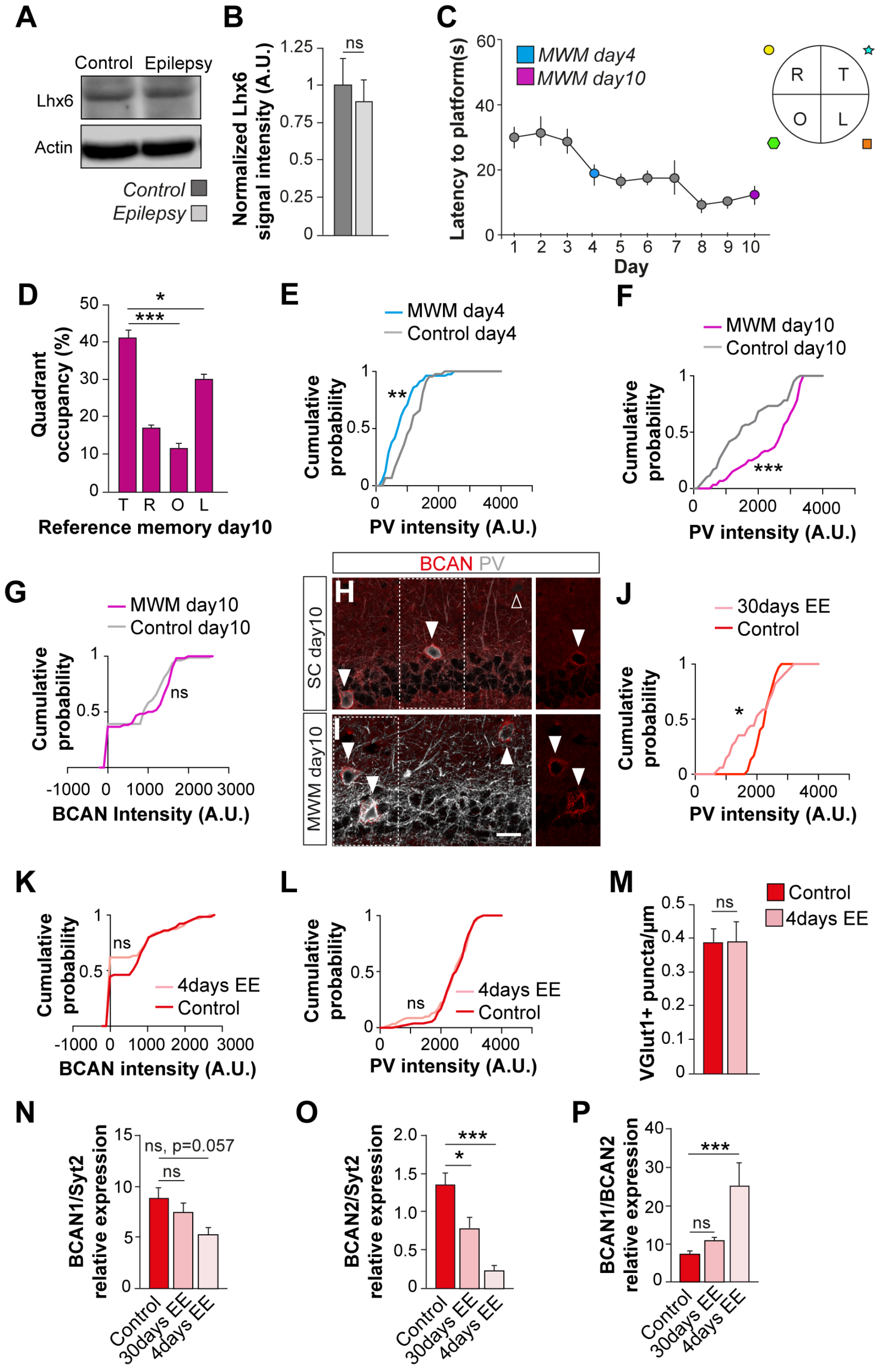

Figure S7

Favuzzi et al.

Figure S7. Experience can modify PV and Brevican expression, related to Figure 7

(A and B) Representative immunoblots (A) and analysis (B) of Lhx6 protein levels in hippocampal lysates from epilepsy patients (n = 4) compared to controls (n = 4).

(C) Morris Water maze (MWM) learning curve (symbols indicate spatial cues).

(D) Reference spatial memory on day 10 during the probe test in the Morris Water Maze (MWM) (n = 5 mice).

(E) Cumulative probability plots comparing PV fluorescence intensity levels in control (n = 44 cells, 3 mice) and MWM trained mice (n = 79 cells, 4 mice) at day 4.

(F and G) Cumulative probability plots comparing the PV (F) and Brevican (G) fluorescence intensity levels in control (n = 60 cells, 4 brains) and MWM trained (n = 60 cells, 4 mice) mice after 10 days.

(H and I) Representative images illustrating Brevican levels in the hippocampus of mice that were trained for 10 days in the MWM compared to swimming controls. Full arrowheads show colocalization, open arrowheads show no colocalization. Scale bar, 20 μm.

(J) Cumulative probability plots comparing PV fluorescence intensity levels in control (n = 30 cells, 3 mice) and mice housed in an enriched environment (EE) for 30 days (n = 34 cells, 3 mice).

(K and L) Cumulative probability plots comparing Brevican (K, n = 65 control, 63 EE cells) and PV (L, 183 control, 149 EE cells) fluorescence intensity levels in control (5 mice) and mice housed in an enriched environment (EE) for 4 days (5 mice).

(M) Density of VGlut1+ boutons contacting the soma of PV+ cells in control (n = 3 mice) and mice housed in an enriched environment (EE) for 4 days (3 mice).

(N and O) *Bcan1* (N) and *Bcan2* (O) mRNA expression relative to that of Syt-2 in control (n = 5 mice) and in mice housed in an enriched environment (EE) for 4 (n = 5 mice) and 30 (n = 5 mice) days.

(P) Ratio between the mRNA expression of *Bcan1* and *Bcan2* in control (n = 5 mice) and mice housed in an enriched environment (EE) for 4 (n = 5 mice) and 30 (n = 5 mice) days.

Mann-Whitney test (B, M), Kolmogorov-Smirnov test (E, F, G, J, K, L), and one-way ANOVA (D, N, O, P).

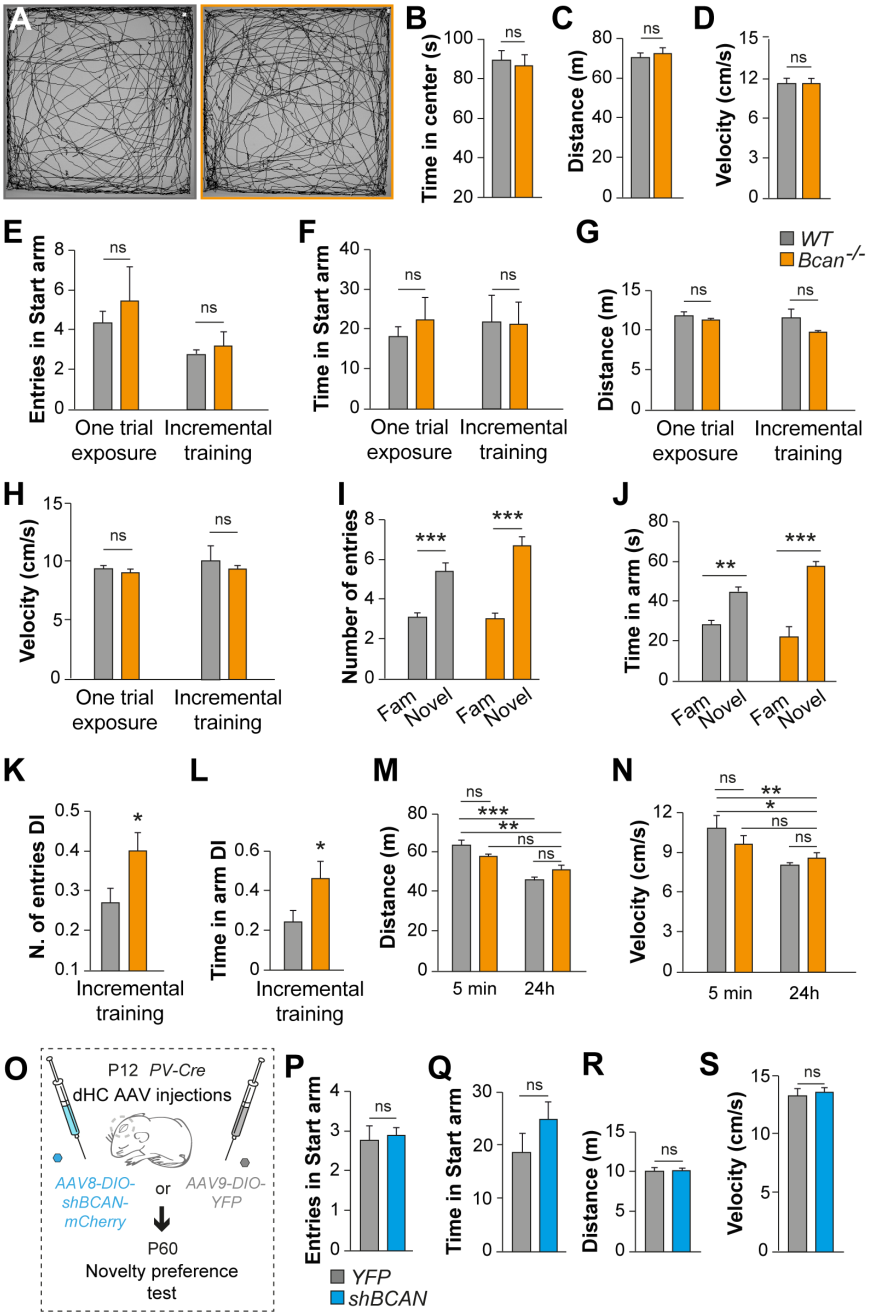

Figure S8

Favuzzi et al.

Figure S8. Brevican deletion does not affect spontaneous locomotor activity, related to Figure 8

(A-D) Behavior of wild type (WT, n = 19) and *Bcan*$^{-/-}$ (n = 20) mice showing representative movement paths of individual mice (A), as well as time spent in the center (B), total distance traveled (C) and velocity (D) across the entire session in the open-field. ns: no significant difference. Note that anxiety and spontaneous locomotor activity are intact in *Bcan* mutant mice.

(E-H) Analysis of the one trial and incremental exposure novelty preference test showing the number of entries (E), time spent (F), distance traveled and velocity (H) in the "start" arm (n = 5 mice per genotype). Number of entries made in the "familiar" and "novel" arms (I), the total time spent in the "familiar" and "novel" arms (J), and the discrimination index for the number of entries (K) and the time spent in the arms (L), for WT (n = 11) and *Bcan*$^{-/-}$ (n = 10) mice.

(M and N) Distance traveled and velocity for WT and *Bcan*$^{-/-}$ mice during the novel object recognition test after 5 minutes ITI (n = 19 WT and n = 20 *Bcan*$^{-/-}$) and 24 hours ITI (n = 18 WT and n = 16 *Bcan*$^{-/-}$).

(O) Schematic illustration of the experiment shown in Figure 8N-Q. *PV-Cre* mice received multiple bilateral injections with one of the indicated AAVs in the dorsal hippocampus at P12 and were tested for the novelty preference.

(P-S) Number of entries, time spent in the "start" arm, distance traveled and velocity for WT (n = 11) and *Bcan* KD mice (n = 13) in the novelty preference test.

One-way ANOVA (E, F, G, H, I, J, M, N), Student t-test (A, K, L, R, S), and Mann-Whitney test (B, C, D, P, Q).

	Brevican+	**Brevican-**	*p* value
Vrest (mV)	-61.77 ± 0.65	-61.85 ± 1.23	0.9510
Rheobase (pA)	135.30 ± 15.62	95.62 ± 18.87	0.0520
First spike latency (ms)	183.40 ± 13.28	168.10 ± 19.17	0.4720
AP Threshold (mV)	-36.35 ± 1.02	-36.43 ± 1.04	0.9560
AP Height (mV)	62.49 ± 1.94	61.11 ± 2.22	0.6530
AP Half-Width (ms)	0.5455 ± 0.0194	0.6462 ± 0.0313	0.0130 (*)
fAHP time (ms)	1.818 ± 0.069	2.123 ± 0.096	0.0130 (*)
fAHP Amplitude (mV)	-26.83 ± 1.11	-24.91 ± 1.79	0.3420
Max FF (Hz)	148.70 ± 6.59	123.70 ± 11.35	0.0480 (*)
Adaptation (%)	19.65 ± 2.15	28.53 ± 3.18	0.0220 (*)
Input resistance (MΩ)	106.3 ± 8.0	155.4 ± 19.0	0.0320 (*)
Time constant (ms)	10.80 ± 0.59	13.95 ± 1.49	0.2600
V-sag (mV)	-2.70 ± 0.34	-4.96 ± 1.17	0.0988
N	22	13	

SUPPLEMENTAL TABLES

Table S1. Summary comparing the intrinsic properties of BCAN+ and BCAN- PV+ interneurons, Related to Figure 2.

Values are provided for each measurement as mean ± SEM. The column to the right indicates the p value (Student's t-test or Mann-Whitney test) of statistical comparisons for each row's variable between BCAN+ and BCAN- cells. Abbreviations: Vrest – Resting Membrane Potential, AP – Action Potential, fAhP – fast-Afterhyperpolarisation, MaxFF – Saturating Firing Frequency, V-sag – voltage relaxation. N indicates number of cells in each condition (for V-sag only, N = 19 Brevican+ and 12 Brevican- cells).

	WT	**Brevican$^{-/-}$**	*p* value
Vrest (mV)	-60.67 ± 0.63	-60.40 ± 0.80	0.7965
Rheobase (pA)	151.20 ± 13.44	145.60 ± 9.92	0.3971
First spike latency (ms)	181.90 ± 11.44	132.40 ± 14.59	0.0084 (**)
AP Threshold (mV)	-36.75 ± 0.54	-40.31 ± 0.57	<0.0001 (***)
AP Height (mV)	61.64 ± 1.08	63.04 ± 1.53	0.223
AP Half-Width (ms)	0.55 ± 0.01	0.61 ± 0.03	0.0227 (*)
fAHP time (ms)	1.85 ± 0.05	2.07 ± 0.08	0.052
fAHP Amplitude (mV)	-25.45 ± 0.73	-21.72 ± 0.58	0.0004 (*)
Max FF (Hz)	158.20 ± 5.28	149.70 ± 6.15	0.3078
Adaptation (%)	20.87 ± 1.37	24.17 ± 1.82	0.1465
Input resistance (MΩ)	118.60 ± 7.14	127.00 ± 8.65	0.453
Time constant (ms)	11.58 ± 0.56	11.97 ± 0.79	0.9433
V-sag (mV)	-3.03 ± 0.37	-3.66 ± 0.4 2	0.1282
N	63	41	

Table S2. Summary comparing the intrinsic properties of wild-type and *Bcan-/-* PV interneurons, Related to Figure 3.

Values are provided for each measurement as mean ± SEM. The column to the right indicates the p value (Student's t-test or Mann-Whitney test) of statistical comparisons for each row's variable between wild-type (WT) and *Bcan-/-* PV interneurons. Abbreviations: Vrest – Resting Membrane Potential, AP – Action Potential, fAhP – fast-Afterhyperpolarisation, MaxFF – Saturating Firing Frequency, V-sag – voltage relaxation. N indicates number of cells in each condition (for V-sag only, N = 48 WT and 40 Brevican$^{-/-}$ cells). The WT group includes all cells in BCAN+ and BCAN- groups (Table S1), plus 14 cells for which Brevican immunostaining was inconclusive.

	WT	**shBrevican**	*p* value
Vrest (mV)	-60.67 ± 0.63	-60.35 ± 1.43	<0.0001 (**)
Rheobase (pA)	151.20 ± 13.44	69.27 ± 11.16	<0.0001 (**)
First spike latency (ms)	181.90 ± 11.44	143.20 ± 13.84	0.0698
AP Threshold (mV)	-36.75 ± 0.54	-42.70 ± 0.96	<0.0001 (**)
AP Height (mV)	61.64 ± 1.08	72.56 ± 1.72	<0.0001 (**)
AP Half-Width (ms)	0.55 ± 0.01	0.99 ± 0.07	<0.0001 (**)
fAHP time (ms)	1.85 ± 0.05	6.12 ± 0.63	<0.0001 (**)
fAHP Amplitude (mV)	-25.45 ± 0.73	17.47 ± 0.99	<0.0001 (**)
Max FF (Hz)	158.20 ± 5.28	86.36 ± 9.54	<0.0001 (**)
Adaptation (%)	20.87 ± 1.37	42.73 ± 3.58	<0.0001 (**)
Input resistance (MΩ)	118.60 ± 7.14	196.30 ± 18.43	<0.0001 (**)
Time constant (ms)	11.58 ± 0.56	14.91 ± 1.13	0.0045
V-sag (mV)	-3.03 ± 0.37	-7.79 ± 0.95	<0.0001 (***)
N	63	22	

Table S3. Summary comparing the intrinsic properties of wild-type and *Bcan* KD (shBrevican) PV interneurons, Related to Figure 4.

Values are provided for each measurement as mean ± SEM. The column to the right indicates the p value (Student's t-test or Mann-Whitney test) of statistical comparisons for each row's variable between wild-type (WT) and *Bcan* KD PV interneurons. Abbreviations: Vrest – Resting Membrane Potential, AP – Action Potential, fAhP – fast-Afterhyperpolarisation, MaxFF – Saturating Firing Frequency, V-sag – voltage relaxation. N indicates number of cells in each condition (for V-sag only, N = 48 WT and 22 *shBrevican* cells). N indicates number of cells in each condition. The WT group is the same as in Table S2.

Variable	***Genotype***	***N***	***Mean***	***SEM***	***Test***	***p value***	***Multiple Comp. vs Bcan-/-***
Vrest (mV)	**Bcan -/-**	53	-58.30	0.85	One-way ANOVA	0.2996	
	Bcan1 rescue	13	-59.40	1.42			
	Bcan2 rescue	32	-60.50	1.21			
Rheobase (pA)	**Bcan -/-**	53	154.00	10.80	Kruskal-Wallis test	0.4214	
	Bcan1 rescue	13	189.00	27.10			
	Bcan2 rescue	32	152.00	13.10			
First spike latency (ms)	**Bcan -/-**	53	139.00	13.50	One-way ANOVA	0.5983	
	Bcan1 rescue	13	112.00	28.30			
	Bcan2 rescue	32	147.00	16.60			
AP Threshold (mV)	**Bcan -/-**	53	-40.80	0.57	One-way ANOVA	0.5876	
	Bcan1 rescue	13	-40.50	0.90			
	Bcan2 rescue	32	-39.90	0.61			
AP Height (mV)	**Bcan -/-**	53	64.10	1.33	One-way ANOVA	0.5418	
	Bcan1 rescue	13	64.40	2.76			
	Bcan2 rescue	32	61.90	1.47			
AP Half-Width (ms)	**Bcan -/-**	53	0.62	0.02	Kruskal-Wallis test	0.758	
	Bcan1 rescue	13	0.59	0.02			
	Bcan2 rescue	32	0.62	0.02			
fAHP time (ms)	**Bcan -/-**	53	2.40	0.19	Kruskal-Wallis test	0.0001	
	Bcan1 rescue	13	2.82	0.35			0.0257 (*)
	Bcan2 rescue	32	2.83	0.16			0.0001 (***)
fAHP Amplitude (mV)	**Bcan -/-**	53	-20.80	0.61	One-way ANOVA	0.0309	
	Bcan1 rescue	13	-17.90	0.65			0.0402 (*)
	Bcan2 rescue	32	-19.50	0.48			0.2161
Max FF (Hz)	**Bcan -/-**	53	138.00	6.56	One-way ANOVA	0.9467	
	Bcan1 rescue	13	134.00	11.80			
	Bcan2 rescue	31	138.00	7.76			
Adaptation (%)	**Bcan -/-**	53	-19.30	2.00	One-way ANOVA	0.0183	
	Bcan1 rescue	13	-30.80	3.96			0.0219 (*)
	Bcan2 rescue	31	-25.70	2.62			0.0526
Input Resistance (MΩ)	**Bcan -/-**	53	130.00	8.82	Kruskal-Wallis test	0.4686	
	Bcan1 rescue	13	122.00	16.20			
	Bcan2 rescue	32	143.00	11.50			
Time constant (ms)	**Bcan -/-**	53	13.00	0.94	Kruskal-Wallis test	0.6804	
	Bcan1 rescue	13	12.30	1.11			
	Bcan2 rescue	32	11.30	0.88			
V-Sag (mV)	**Bcan -/-**	40	-3.66	0.42	Kruskal-Wallis test	0.6034	
	Bcan1 rescue	13	-5.03	1.03			
	Bcan2 rescue	32	-3.97	0.49			

Table S4.

Summary comparing the intrinsic properties of *Bcan-/-*, BCAN1 and BCAN2 overexpressing PV interneurons, Related to Figure 5.

Values are provided for each measurement as mean ± SEM. The columns to the right indicate the p value (one-way ANOVA or Kruskal–Wallis test) of statistical comparisons for each row's variable between *Bcan*-/-, BCAN1, and BCAN2 overexpressing PV interneurons followed by Holm-Sidak's multiple comparison test when significant differences were found. Abbreviations: Vrest – Resting Membrane Potential, AP – Action Potential, fAhP – fast-Afterhyperpolarisation, MaxFF – Saturating Firing Frequency, V-sag – voltage relaxation. N indicates number of cells in each condition. The *Bcan*-/- group includes all cells in *Bcan*-/- group from Table S2, plus 12 YFP+HA- cells from the injected mice.

Oligonucleotides		Sequence
shBCAN	Fw	CTAGGCAAGCAGAACCGCTTCAATG CCTGACCCACATTGAAGCGGTTCTGTTGCTTTTTG
	Rv	AATTCAAAAAG CAAGCAGAACCGCTTCAATGTGGGTCAGGCATTGAAGCGGTTCTGCTTGC
Bcan1 ISH probe	Fw	TGCACCCCTGAGGAGCAAGAC
	Rv	CGGGTAAAACCTGAGGCCC TTGTG
Bcan2 ISH probe	Fw	GTAATTCTGCTGAAGGCTCAA
	Rv	TGGGTACAAAGCAGTTTAATACAG
HA tag sequence	Fw	TCTAGAGCCACCATGATACCACTGCTTCTGTCCCTGCTGGCCGCTCTGGT
	Rv	TTGGGTCAGGACCAGAGCGGCCAGCAGGGACAGAAGCAGTGGTA TCATGGTGGCCTAGAA
Bcan signal peptide	Fw	CCTGACCCAAGCCCCTGCCGCCCTCGCTGA TTACCCATACGATGTTCCAGATTACGCTAGATCTA
	Rv	AGATCTAGCGT AATCTGGAACATCGTATGGGTAATCAGCGAGGGCGGCAGGGGC
Bcan1 qPCR	Fw	CTATGTTTGCCAGGCTATGGGGG
	Rv	TGCCTCCTCCCAACTCCTTCGTG
Bcan2 qPCR	Fw	GTCCTGGCAGGCACCTCAGTG
	Rv	GCATTGAGCCTTCAGCAGAA TTAC
Syt2	Fw	ACGTGCCCACAGCTGGGAAGCTC
	Rv	GTCTCTTACCGTTCT GCATCAGG
Gfap	Fw	GGGACAACTTTGCACAGGACCTC
	Rv	GGTGGCTTC ATCTGCCTCCTGTC

Table S5. Oligonucleotide sequences. Related to Key Resources Table and STAR Methods.